nature research

https://doi.org/10.1038/s41551-020-00644-2

Supplementary information

Systemic tumour suppression via the preferential accumulation of erythrocyte-anchored chemokine-encapsulating nanoparticles in lung metastases

In the format provided by the authors and unedited

Table of contents

Supplementary Methods

Materials

All chemicals and reagents were obtained from Sigma Aldrich (MO, USA) and used without further purification, unless otherwise mentioned. PLGA (50:50 acid-end, 50:50 ester-end, 85:15 ester-end, and 65:35 acid-end) was purchased from Sigma-Aldrich (MO, USA). mPEG-PLGA was purchased from PolySciTech (IN, USA). CXCL10/IP-10, IL-2, IL-12, IL- 15, and GM-CSF were obtained from PeproTech (NJ, USA). Nunc™ Lab-Tek™ II Chamber Slide™ System, cell staining buffer, G418 (Geneticin), mouse IP-10 ELISA kit, Alexa Fluor 647 Ovalbumin, Alexa Fluor 750 NHS reagent, Alexa Fluor 647 NHS reagent, phosphate buffered saline(1X), Axygen™ 1.5mL Self-Standing Screw Cap Tubes, Pierce™ LAL Chromogenic Endotoxin Quantitation Kit was obtained from Thermo Fischer Scientific (MA, USA). Human whole blood and serum was obtained from BioIVT (NJ, USA). Xenolight-D-luciferin potassium salt was obtained from Perkin Elmer (MA, USA). Lithium heparin coated microtainer tubes were obtained from BD medical technology (MA, USA). LEGENDplex™ Mouse Inflammation Panel with Filter Plate, recombinant mouse RANTES (Cat no: 594208), and anti-ICAM-1 antibody (Cat no: 116102, Clone: YN 1/1.7.2; Cat no:353102, Clone: HA58) was obtained from BioLegend (CA, USA). Tissue dissociation tubes and lung dissociation kit were obtained from Miltenyi Biotec (Germany). Tissue Tek OCT compound was obtained from Sakura Finetek (CA, USA). 0.9 % saline solution was obtained from Teknova (CA, USA). Paraformaldehyde was obtained from Electron Microscopy Sciences (PA, USA). Surgical equipment was obtained from Braintree Scientific, Inc. (MA, USA). Clodrosome® was obtained from Encapsula NanoSciences (TN, USA).

Preparation of PLGA nanoparticles with different material properties

PLGA nanoparticles with different material properties were prepared using a double emulsion method. Briefly, 20 mg of different PLGA polymers (50:50 acid-end, 50:50 ester-end, 85:15 ester-end, and 65:35 acid-end) was dissolved in 1 mL of dichloromethane to form the organic phase. 200 µL of PBS containing Alexa Fluor 750 or Alexa Fluor 647 labeled ovalbumin was added to the organic phase and thoroughly mixed with vertex. The mixture was briefly sonicated in a water-bath sonicator and then added dropwise to 11 mL of 1.5 % polyvinyl alcohol (PVA) solution under constant stirring. The entire mixture was probe-sonicated at 50% amplification for a total of 40 seconds (20 seconds pulse on, 10 seconds pulse-off, and then 20 seconds pulse on). The formed particles were kept under constant stirring overnight to remove the organic solvents. The particles were centrifuged at 12,000 *g* for 10 mins. The nanoparticles were washed for a total of two washes with deionized water to sufficiently remove excess surface PVA before their final resuspension in PBS. To characterize the physicochemical properties of nanoparticles, after washing, the particles were resuspended in de-ionized water and assessed for their size, zeta potential and polydispersity index using dynamic light scattering (Malvern Zen3600, PA, USA).

In vitro drug release study

CXCL10 containing nanoparticles (ImmunoBait) were resuspended in 1 mL PBS, FBS and complete medium (DMEM + 10% FBS) and incubated at 37 °C on a tube revolver. At regular time points, the particles were centrifuged at 12,000 *g* for 10 mins and the supernatant was collected for analysis. The particles were further resuspended in 1mL of fresh release media and incubated at 37 °C until the next time point. Samples were taken at 1, 2, 4, 6, and 12 h after starting the incubation. The cumulative release in each release media was quantified using ELISA. In addition, the released CXCL10 chemokine was characterized by MALDI-TOF and Circular Dichroism Spectrophotometer to detect any molecular weight and structural changes.

Nanoparticle internalization studies

Nanoparticle internalization was confirmed using confocal microscopy. For flow cytometry analysis, 2 x10^5 HLMVEC cells were plated in a 2-well chamber and allowed to adhere overnight. Chambers were then aspirated, and 1 ml of fresh media was added to each well. 30 μg of Alexa Fluor 647 labeled nanoparticles were added to each well and allowed to incubate for 20 mins or 6 h at 37 °C in an incubator. After the stipulated time points, media in the wells was completely aspirated and washed 3 times with PBS and the cells were fixed with 4% paraformaldehyde. After wash, cells were stained with Fluoroshield™ with DAPI and a coverslip was mounted. These cells were analyzed by confocal microscope (Upright Zeiss LSM 710 NLO ready).

Erythrocyte PEGylation

PEGylation of erythrocytes were performed according to a previously reported method from our group.[1]

In brief, erythrocytes were incubated in PBS that contains 10 mg/mL Cyanuric chloride-functionalized 5-kDa m-PEG (C-mPEG) for 30 mins. The C-mPEG formed covalent bonds with the amine groups on erythrocyte surface. Unreacted C-mPEG was eliminated by pelleting the erythrocytes by centrifugation followed by two washes using PBS. PEGylated erythrocytes were resuspended in PBS for use.

Hitchhiked erythrocyte characterizations and biocompatibility

Hitchhiking efficiency and the nanoparticles loaded on erythrocytes were determined using fluorescence measurements. For quantification using fluorescence, 25 μL of erythrocytes were lysed using deionized water and the nanoparticle content was quantified using fluorescence on a plate reader (Tecan Safire 2®, Switzerland). Nanoparticle attachment to erythrocytes was confirmed using scanning electron microscopy (Zeiss FESEM Supra 55VP, Zeiss FESEM Ultra 55, Germany). Briefly, the hitchhiked erythrocytes were fixed using 2.5% glutaraldehyde solution and washed in an increasing ethanol gradient before being chemically dried using hexamethyldisilazane (HMDS). Finally, the samples were sputter coated (EMT 150T ES metal sputter coater, PA USA) prior to imaging. For biocompatibility studies, osmotic fragility and agglutination assays were carried out as previously described.[2]

***In vitro* shear studies**

Nanoparticles were labeled by Alexa Fluor 647-OVA and used for the shear studies. For low shear studies, hitchhiked murine erythrocytes were incubated in 1 mL of FBS on a tube revolver at 12 rpm at 37° C. After incubation for 20 mins, the cells were pelleted by centrifugation at 250 *g* for 5 mins and resuspended to 10 % v/v in 1X PBS. 25 μL of erythrocytes were then lysed using deionized water and the remaining drug content was quantified using fluorescence on a plate reader (Tecan Safire 2®, Switzerland).

For high shear studies, hitchhiked murine erythrocytes were incubated in 10 mL of FBS. A rotatory shear (2 Pa, 6 Pa, or 10 Pa) was applied to erythrocytes in serum using a cylindrical couette viscometer (1 mm gap, AR-G2 rheometer, TA instruments) for 20 mins. The samples were maintained at 37 °C during the application of shear using a water jacket. These conditions simulate high shear physiological environment. After 20 mins, the cells were pelleted by centrifugation at 250 *g* for 10 mins and resuspended to 10 % v/v in 1X PBS. 25 μL of erythrocytes were then lysed using deionized water and the remaining nanoparticle content was quantified using fluorescence on a plate reader (Tecan Safire 2®, Switzerland) and confirmed using scanning electron microscopy (Zeiss FESEM Supra 55VP, Zeiss FESEM Ultra 55, Germany).

Nanoparticle distribution within the lungs

For nanoparticle distribution within the diseased lungs, 1 x 10^6 4T1-Luc cells were injected orthotopically into the left mammary fat pad of female Balb/c mice. 19 days after inoculation, tumours were surgically resected. 28 days after tumour resection, mice were injected with 17 μg Alexa Fluor 647 labeled nanoparticles with anti-ICAM-1 and erythrocyte hitchhiked fluorescent nanoparticles with anti-ICAM-1. 20 mins after the injection, the mice were euthanized, and the intact lungs were collected. Lungs were washed twice with cold 1X PBS before being fixed in a 4 % paraformaldehyde solution overnight. The fixed lungs were then frozen in Tissue Tek OCT compound (Sakura Finetek, CA, USA) and sectioned using a cryostat (Leica CM1950, Germany). The sectioned tissue was mounted using Fluoroshield® to stain for DAPI (Ex/Em 340/488 nm) and were analyzed using confocal microscope (Upright Zeiss LSM 710 NLO ready, Germany).

***In vivo* biodistribution studies in healthy mice**

For biodistribution study with different PLGAs, healthy female Balb/c mice were used. Alexa Fluor 750-OVA encapsulating NPs and hitchhiked NPs (n=3 for all groups) at a dose containing 17 μg NPs were injected intravenously into the tail vein. Mice were sacrificed at 20 mins after the injection and organs (liver, lungs, spleen, kidneys, heart, brain and blood) were harvested for further processing. For comprehensive biodistribution, Alexa Fluor 750-OVA encapsulating NPs, hitchhiked NPs, Alexa Fluor 750-OVA encapsulating NPs with anti-ICAM-1 and hitchhiked NPs with anti-ICAM-1 (n=3 for free NPs and n=6 for hitchhiked NPs) were injected intravenously into the tail vein. Mice were sacrificed at 20 mins, 2 h, 6 h, and 24 h after the injection and organs (liver, lungs, spleen, kidneys, heart, brain and blood) were harvested for further processing. For processing, 1 mL of cold RIPA lysis buffer (1X) was added to each organ and the organs were homogenized using a high shear homogenizer (IKA T-10 Basic ®Ultra turrax, Germany) and the nanoparticle content was quantified by fluorescence measurement on a plate reader (Tecan Safire 2®, Switzerland).

Late-stage efficacy in a breast cancer spontaneous lung metastasis model

For the late-stage efficacy, spontaneous lung metastasis model was established by orthotopic injection of 1 x 10^6 4T1-Luc into the left mammary fat pad of female Balb/c mice. 32 days after the inoculation, tumours were surgically resected. Treatments were given starting one week after surgery. Four injections were given every two days. The injected doses are same as in the early-stage model. Two days after the last injection (on day 50), the mice were euthanized, intratracheally injected with India ink solution and the lungs were excised and fixed using Feket's solution as previously describe.[3] The fixed lungs were used for counting of the surface nodules.

Efficacy study on the B16F10 melanoma lung metastasis model

B16F10-Luc cell line expressing luciferase was obtained from Imanis Life Sciences (MN, USA). B16F10-Luc cells were cultured in a humidified incubator maintained at 37 °C and 5 % CO_2. They were cultured in DMEM media supplemented with 10 % FBS, 1% Pen-Strep and 1 μg/mL puromycin.

The experimental melanoma lung metastasis model was established by intravenously (tail vein) injecting 1 x 10^5 B16F10-Luc cells into male C57BL/6 mice. ImmunoBait or hitchhiked ImmunoBait (EASI) was used in the efficacy study. Four injections were given over 9 days, i.e. on day 1, 4, 7, and 9 following tumour inoculation. The injected formulations contained 2.5 μg of CXCL10 chemokine. On day 17, blood was collected using a submandibular bleeding method. Blood and serum samples were submitted to IDEXX BioAnalytics (North Grafton, MA) for hematological and serum chemistry analysis. On the same day (day 17), the mice were euthanized, intratracheally injected with India ink solution and the lungs were excised and fixed using Feket's solution. The fixed lungs were used for counting of the surface nodules**.**

For the tumour rechallenge study, the melanoma lung metastasis was established using the same method as described in the efficacy study. Mice received the same doses of treatments as in the efficacy study. 10 days after the last injection of therapies (on day 19), 5 x 10^5 B16F10-Luc cells were subcutaneously administered into the mammary fat pad of disease mice or age matched healthy mice that received no prior tumour inoculations. Tumour growth was measured every other day.

Supplementary Results

Mechanism of anchoring of nanoparticles to erythrocytes

Our hypothesis is that 1) the hitchhiking process is contact dependent, i.e. nanoparticles should be able to approach the RBC membrane clearly, spread the membrane and eventually get lodged into it, primarily due to non-covalent forces. 2) Post the membrane spreading, the particles are able to remain attached to the RBC membrane due to thermodynamic equilibrium between the membrane surface tension and non-covalent forces between the membrane and nanoparticle surface, including electrostatic interactions, hydrophobic interactions, and hydrogen bonding.

To test the first hypothesis, we first conjugated PEG onto the surface of erythrocytes to inhibit the surface contact of nanoparticles and erythrocyte membrane. According to **Fig. S1b**, the PEG on the RBC surface hindered the approach of nanoparticles towards the RBC, thereby reducing the hitchhiking efficiency by 50 %. These data indicate that the anchoring of nanoparticles to erythrocyte surface is indeed contact dependent. Next, we fixed the erythrocytes to inhibit the spreading of erythrocyte membranes. As shown in **Fig. S1a**, in the case of fixed RBCs, the hitchhiking efficiency of RBCs dramatically reduced to zero, indicating that if the nanoparticles are not able to spread the membrane, they are unable to bind to the RBC membrane. This study suggests that the anchoring of nanoparticles requires membrane spreading, i.e. if the approach is hindered or the membrane chemically fixed to prevent stretching, the hitchhiking process gets drastically affected.

To test the second hypothesis, we conducted hitchhiking experiments in serum rather than PBS to inhibit the overall non-covalent interactions between nanoparticles and erythrocyte membranes. The serum proteins would form corona around the nanoparticles and also cover RBCs thereby masking/reducing overall nanoparticle- RBC interactions. As shown in **Fig. S1c**, in a sharp contrast to PBS, utilizing serum as the hitchhiking media reduced hitchhiking efficiency by 60 %, indicating non-covalent interactions are largely responsible for the holding of nanoparticles onto erythrocyte membranes.

We hypothesize that the actual non-covalent forces responsible for holding the nanoparticles in place once the RBC membrane spreads include electrostatic interactions, hydrophobic interactions, and hydrogen bonding. In our previous study, we reported that positively charged nanoparticles bound to erythrocytes at a super high efficiency (> 40%), suggesting the electrostatic interactions play a critical role in binding of nanoparticles to erythrocytes[4]. This is understandable because the erythrocyte membrane carries negative charge. However, negatively charged nanoparticles could also efficiently bind to erythrocytes, in which case electrostatic interactions do not involve. We hypothesize that hydrophobic interactions between nanoparticles and erythrocyte membranes are the major players in this case to hold nanoparticles in place. To test this hypothesis, we inhibited the hydrophobic interactions by covering the nanoparticles with hydrophilic PEG. As shown in **Fig. S1d**, in the case of PEG modified nanoparticles, the overall hitchhiking efficiency reduces by almost 75%, indicating that hydrophobic forces are vital in order for the process to happen efficiently. Apart from electrostatic and hydrophobic interactions, we hypothesize that other non-covalent

interactions such as hydrogen bonding also plays a significant role in holding nanoparticles on erythrocyte membranes. To test this hypothesis, we compared the binding of ester-end and acid-end PLGA nanoparticles (of same composition) to erythrocytes. Ester-end PLGA nanoparticles are more hydrophobic while acid-end nanoparticles are able to form hydrogen bonding with cell membranes. As shown in **Fig. S1e**, when using ester-end nanoparticles instead of acid-end nanoparticles, the hitchhiking efficiency surprisingly reduced by 25%. This was unexpected, given that hitchhiking primarily was believed to be dominated by hydrophobic forces. This result indicates that H-bonding also controls hitchhiking to certain extent.

In summary, based on our data, we believe that the anchoring of nanoparticles to erythrocytes can follow the proposed mechanism: the nanoparticles approach the RBC membrane, and in absence of competitive shielding proteins/forces, spread the RBC membrane in a contact dependent manner. After this, nanoparticles are held in place due to non-covalent forces of attraction (electrostatic interactions, hydrophobic forces, and H-bonding) between the RBC membrane and the nanoparticle surface.

Detachment of PLGA nanoparticles with different materials properties from erythrocytes

Our mechanism study (**Fig. S1**) suggest that both hydrophobic interactions and hydrogen bonding contribute to the binding of nanoparticles to erythrocytes. Under non-shear conditions, both H-bonding and hydrophobic interactions are sufficiently strong to hold nanoparticle on erythrocytes. PLGA-d has balanced hydrophobicity and hydrogen bonding ability, and thus show highest affinity to erythrocytes under non-shear conditions. However, H-bonding is relatively weaker than hydrophobic interactions. Therefore, under shear conditions, the weak hydrogen bond is easier to break down and leads to dislodgement of nanoparticles from erythrocytes. Since hydrogen bonding is a dominant force for PLGA-d binding to erythrocytes, more nanoparticles were dislodged from erythrocytes under shear conditions (**Fig. S4**).

Detachment of ImmunoBait from erythrocytes *in vivo*

To further characterize the hitchhiked erythrocyte system *in vivo*, we double labeled the system in which the carrier erythrocytes were labeled by CellTrace™ Far Red and the nanoparticles were labeled by FITC (**Fig. S6a**). We injected the double labeled hitchhiked erythrocyte system and collected the blood at different time points and analyzed the hitchhiked system by flow cytometry. As shown in in **Fig. S6b** and **Fig. S6d**, the carrier erythrocytes remained in the blood for at least 24 hours. In contrast, as shown in **Fig. S6c** and **Fig. S6e**, most of the nanoparticles on the carrier erythrocytes (> 95%) were quickly detached from the carrier erythrocytes in < 5 min and the biodistribution data shown in **Fig. S6f** suggested the detached nanoparticles were most deposited in the lung. The data shown in **Fig. S6** together with our previous studies[5] suggest that nanoparticles anchored on erythrocytes are quickly sheared off at the first capillary bed they hit. In the case of intravenous injection, lung is the first capillary rich organ that the carrier erythrocytes see and hence deposit the most anchored nanoparticles there instead of other organs.

Assessment of the safety of EASI

To evaluate the toxicity of EASI, we first assessed the cytokine profiles in the lung and blood after three doses of EASI treatments. One day after the last dose, mice were euthanized and pro-inflammatory cytokine levels of the lung and serum were measured. As shown in **Fig. S24a**, EASI led to overall elevated levels of pro-inflammatory cytokines in the lung compared to the saline group. However, further analysis (**Fig. S24b-d**) suggests that the concentration of key acute pro-inflammatory cytokine markers of the EASI group, including TNF-α, IL-6, and IL-1β, was not

significantly increased as compared to that of the saline group, suggesting the absence of an acute inflammatory response in the lung. In addition, pro-inflammatory cytokine profiles of the serum (**Fig. S27**) further revealed that no obvious systemic acute inflammation was caused by the treatment by EASI, as the concentration of key pro-inflammatory cytokine markers (TNF-α, IL-6, and IL-1β) was not significantly different from that of the saline group.

To further assess the safety of EASI, we performed a hematological and serum chemistry analysis on mice after being treated with four doses of EASI. Blood was collected 7 days after the last dose of EASI. As shown in **Fig. S28b**, all of the measured hematological parameters were within the established normal range and no significant differences were noted between the EASI and saline group. Similarly, as shown in **Fig. S28a**, no significant difference was observed for serum chemistry (liver, kidney, and toxicity panels) parameter levels between EASI and saline, indicating the lack of detectable systemic toxicity.

The safety of EASI was further evaluated by histological analysis of major organs after mice being treated with four doses of EASI. As shown in **Fig. S29**, no detectable damage was observed on the healthy tissue of the metastatic lungs following the treatment by EASI. This suggests that at the dose that is effective to suppress lung metastasis, EASI did not have obvious safety issue to the healthy lung tissue. In addition, EASI did not cause damage to other tested organs, including liver, spleen, kidney, and heart (**Fig. S30**). Our safety data, including cytokine profiles in the lung and serum, hematological and serum chemistry analysis, and histological analysis, collectively, demonstrate that there is no obvious toxicity associated with EASI.

Supplementary Tables

Table S1. Properties of four PLGA candidates

	PLGA-a	**PLGA-b**	**PLGA-c**	**PLGA-d**
L: G ratio*	50:50	50:50	85:15	65:35
End-group	Ester-end	Acid-end	Ester-end	Acid-end
Diameter (nm)	204.5 ± 9.1	189.5 ± 7.8	200.6 ± 9.3	172.4 ± 8.0
Zeta-potential (mV)	-19.5 ± 0.7	-28.0 ± 1.7	-9.2 ± 0.4	-28.4 ± 1.0

* Molar ratio of lactic acid to glycolic acid in the polymer. Data of diameter and zeta-potential are presented as mean ± s.d. (n=5 independent samples).

Supplementary Figures

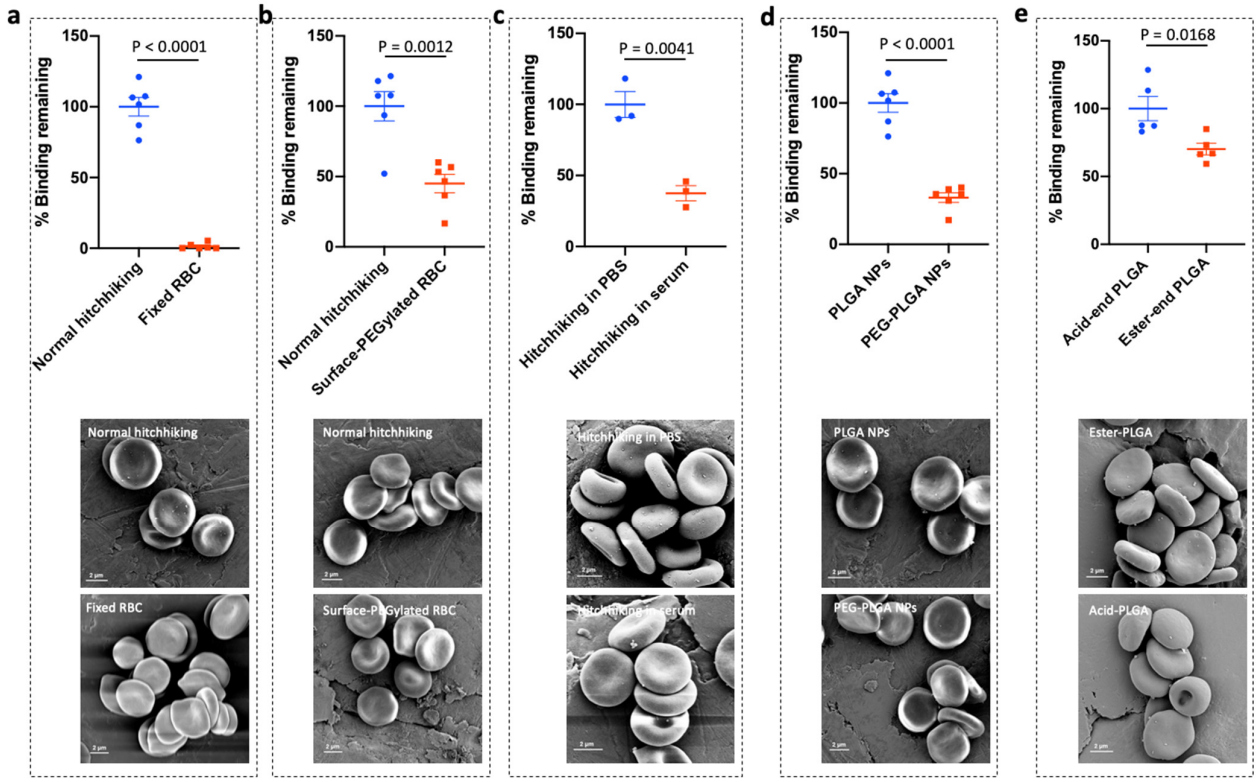

Fig. S1. Mechanisms of nanoparticles anchoring to erythrocytes
Relative binding efficiency and representative SEM images of nanoparticles anchoring to erythrocytes under different conditions. (**a**) When erythrocytes were fixed by 2.5% glutaraldehyde. (**b**) When the surface of erythrocytes was PEGylated. (**c**) When the hitchhiking was conducted in serum. (**d**) When PLGA NPs were PEGylated. (**e**) When PLGA NPs had different surface end (different hydrogen bonding capability). Statistical analysis: two-tailed student's t test. Data in (**a-e**) are presented as mean ± s.e.m.. The "Normal hitchhiking" group in (**a**) and the "PLGA NPs" group in (**d**) are the same.

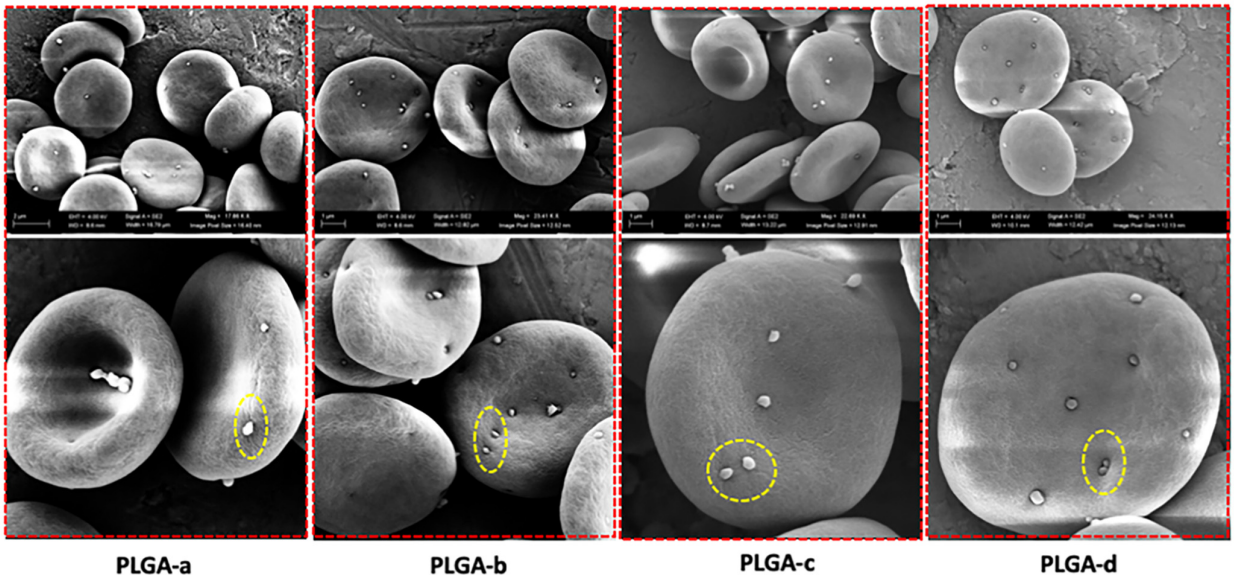

Fig. S2. Scanning electron microscopic (SEM) images of mouse erythrocytes carrying different PLGA nanoparticles

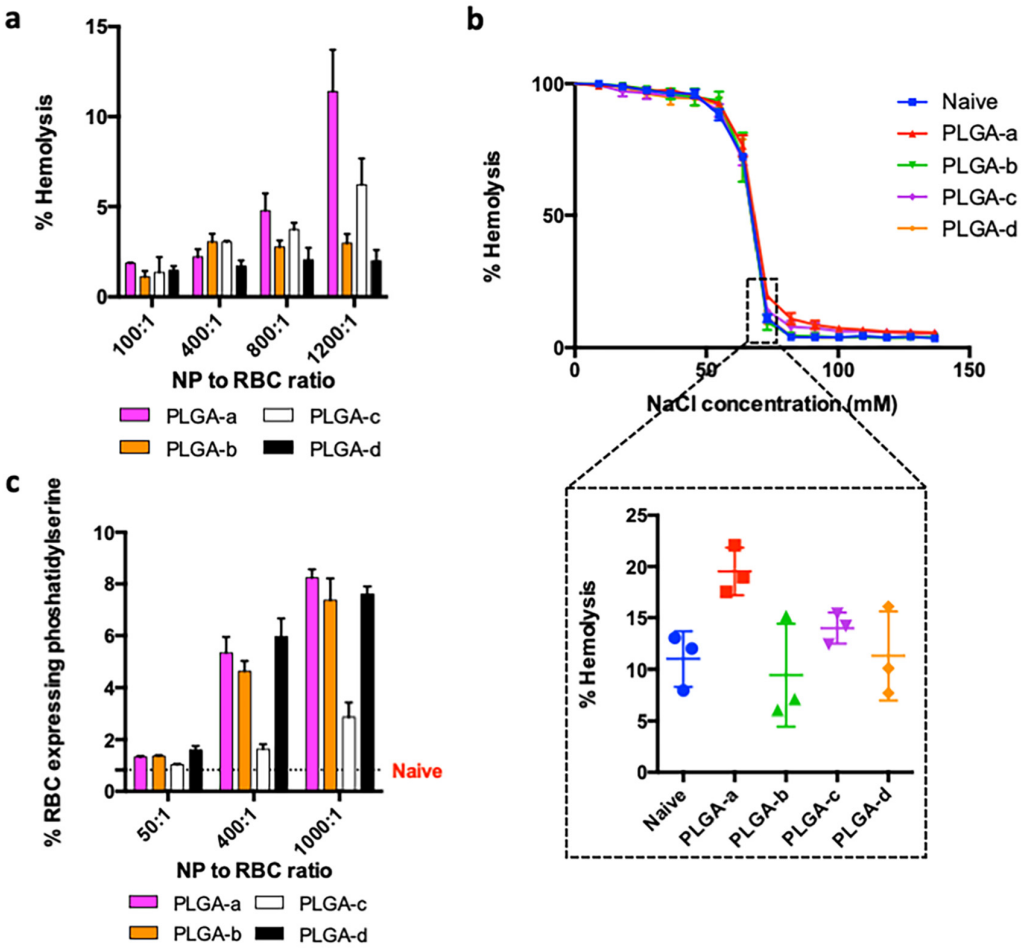

Fig. S3. Effect of different PLGA nanoparticles on the carrier erythrocytes

(**a**) Percent carrier erythrocytes lysed during the hitchhiking process (n=3 independent samples). (**b**) Osmotic fragility (hemolysis during osmotic shock) of the carrier erythrocytes with different PLGA nanoparticles hitchhiked on them (n=3 independent samples). The enlarged panel shows the percent hemolysis of carrier erythrocytes at a NaCl concentration of 72.5 mM. (**c**) Percent carrier erythrocytes expressing phosphatidylserine on their surface after being hitchhiked by different PLGA nanoparticles (n=3 independent samples). Data in (**a, b, c**) are presented as mean ± s.e.m..

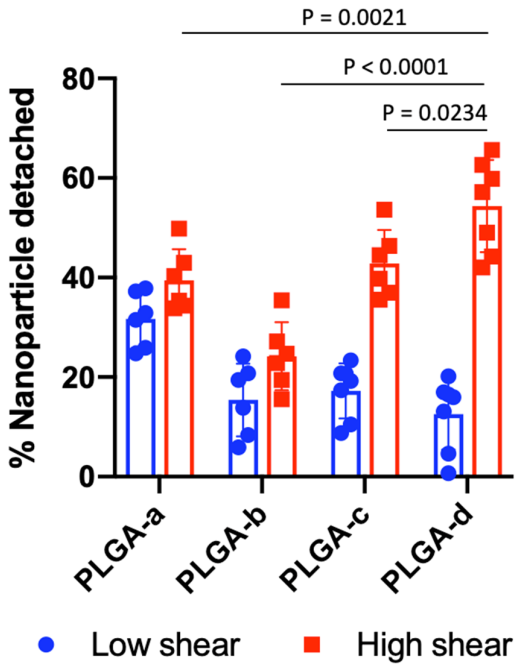

Fig. S4. Percent nanoparticles detached from the carrier erythrocytes under *in vitro* shear conditions
Erythrocytes with different PLGA nanoparticles hitchhiked on them were sheared for 20 mins using a rheometer at a high rotary stress (6 Pa) (n=6-7 independent samples). Low shear indicates a rotary stress the carrier erythrocyte experienced during rotation using a revolver at 12 rpm/min. Data in are presented as mean ± s.e.m. Statistical analysis: two-way ANOVA followed by Tukey's HSD test.

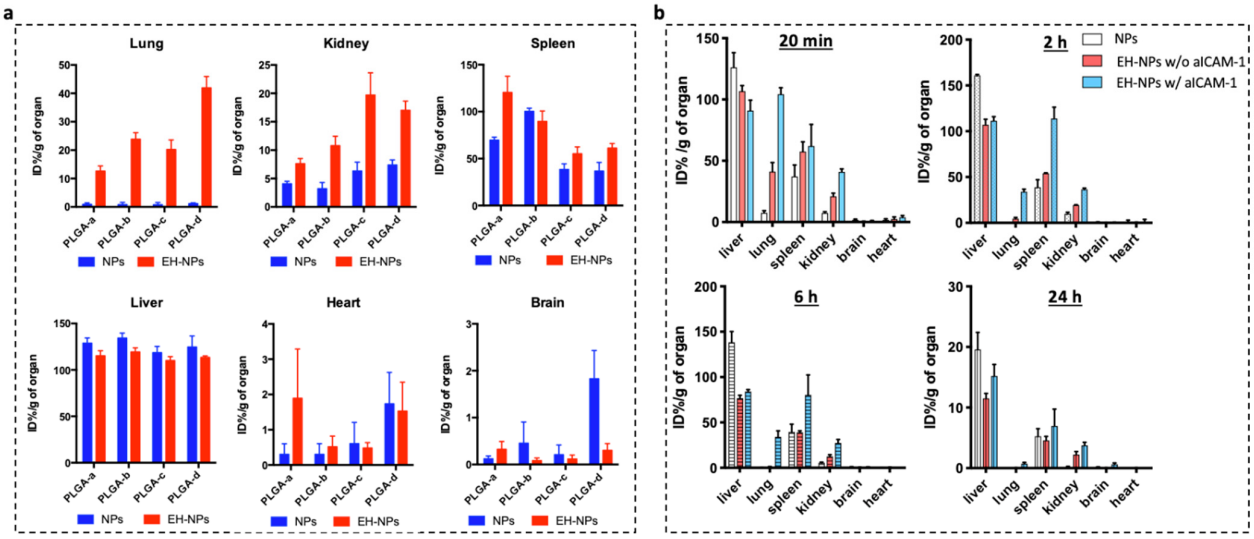

Fig. S5. Biodistribution of PLGA nanoparticles

(**a**) Biodistribution of different PLGA nanoparticles either in a free form or hitchhiked to erythrocytes 20 min after intravenous administration (n=3 biologically independent animals per group for NPs, n=6 biologically independent animals per group for EH-NPs). (**b**) Biodistribution of hitchhiked PLGA-d nanoparticles with or without anti-ICAM-1 antibody at different time points after intravenous administration (n=3 biologically independent animals per group). Data in (**a, b**) are presented as mean ± s.e.m..

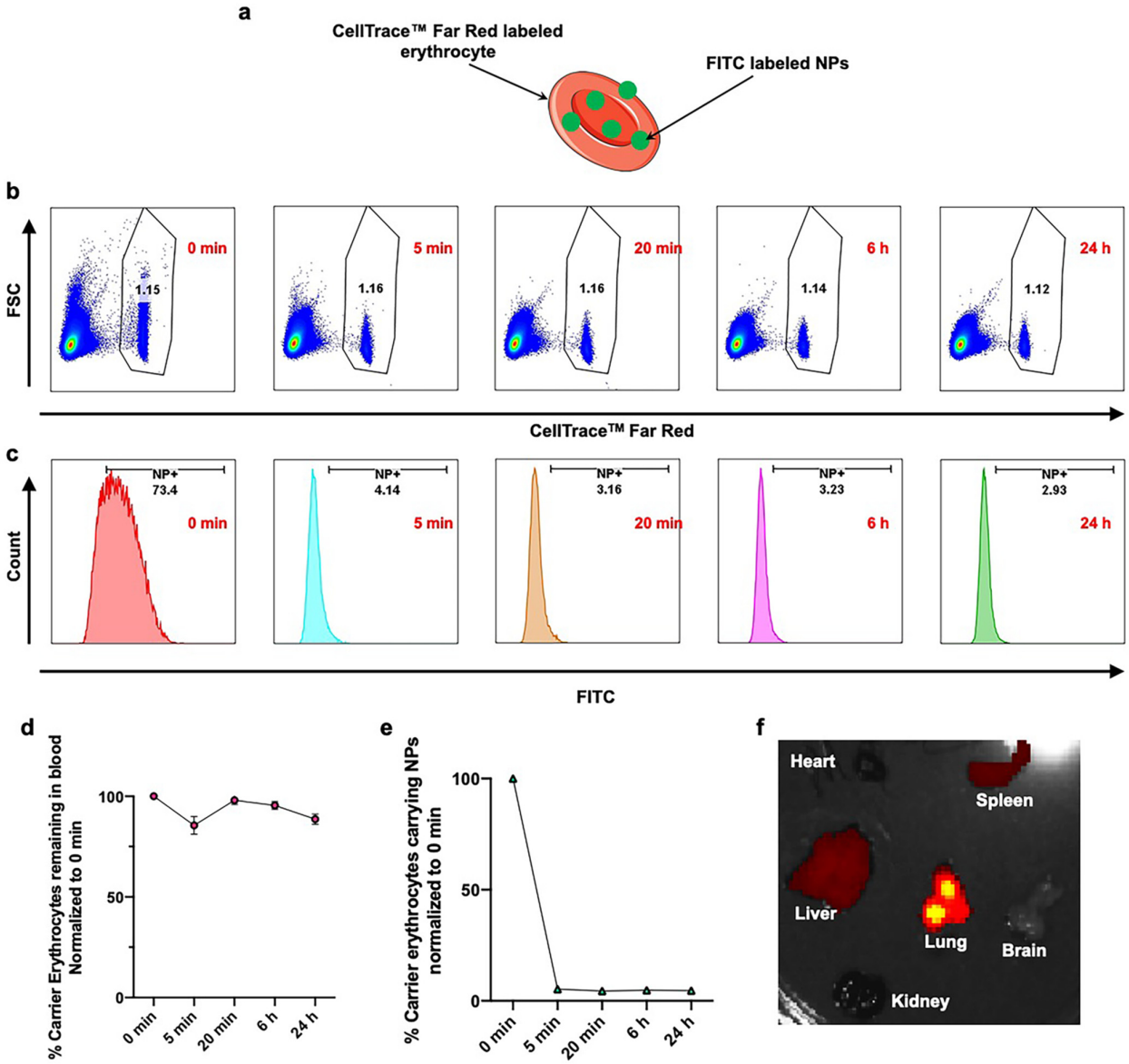

Fig. S6. Characterization of the erythrocyte hitchhiking system in the blood after i.v. administration

(**a**) Schematic illustration of the dual-labeling strategy for the tracking of carrier erythrocytes and nanoparticles. The carrier erythrocytes were labeled with CellTrace™ Far Red and PLGA-d nanoparticles were labeled with FITC. Blood was collected at different time points after i.v. administration of the dual-labeled system. The carrier erythrocytes and the nanoparticles on them were analyzed by flow cytometry. (**b**) Representative flow plots of the blood at different time points (n=3 biologically independent animals per group). (**c**) Representative flow plot of the administered erythrocytes at different time points (n=3 biologically independent animals per group). (**d**) Percentage of the carrier erythrocytes remaining in the blood at different time points as normalized to 0 min (n=3 biologically independent animals). (**e**) Percentage of the carrier erythrocytes carrying hitchhiked nanoparticles at different time points as normalized to 0 min (n=3 biologically independent animals per group). (**f**) IVIS images of organs of mice 5 min after i.v. administration of the erythrocyte hitchhiking system. In (**f**), nanoparticles were labeled by encapsulating AF647 while the carrier erythrocytes were not labeled. Data in (**d, e**) are presented as mean ± s.e.m..

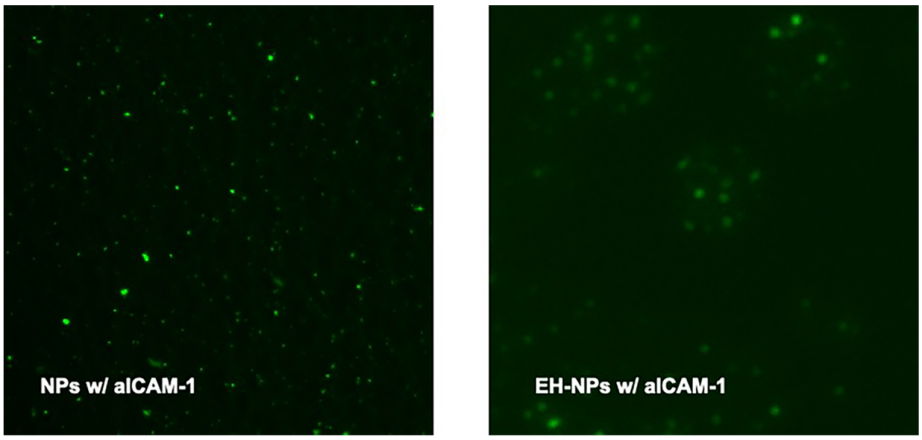

Fig. S7. Verification of the attachment of anti-ICAM-1 antibody (aICAM-1) to nanoparticles
In general, nanoparticles, hitchhiked erythrocyte (EH-NPs), and un-hitchhiked erythrocyte pellets were re-suspended in 0.5 mg/mL anti-ICAM-1 antibody solution for 20 mins. FITC-aICAM-1 was used for imaging and quantification. After incubation, the nanoparticles or hitchhiked erythrocytes were pelleted by centrifugation. The binding efficiency of aICAM-1 to NPs were quantified based on measuring the remaining concentration in the supernatant by FITC fluorescence. Un-hitchhiked erythrocytes were used as a control for quantify aICAM-1 binding on hitchhiked nanoparticles. The above images indicate that aICAM-1 antibody was efficiently attached to free nanoparticles and hitchhiked nanoparticles. Meanwhile, the attachment efficiency of aICAM-1 to free nanoparticles and hitchhiked nanoparticles was 15.4 ± 6.7 μg antibody /mg nanoparticle and 6.5 ± 3.4 μg antibody /mg nanoparticle, respectively.

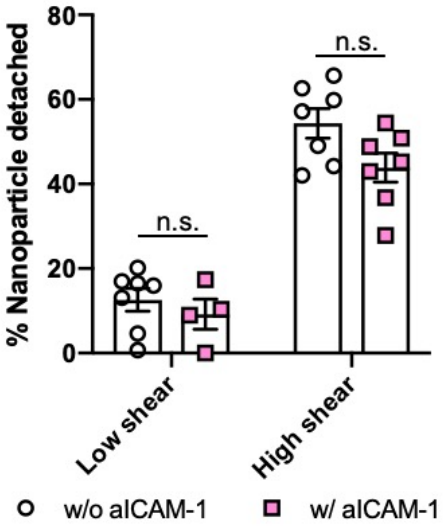

Fig. S8. Effect of the binding of aICAM-1 antibody to EH-NP complex on the detachment of nanoparticles from carrier erythrocytes under shear stress

Erythrocytes with PLGA-d nanoparticles hitchhiked on them w/ or w/o aICAM-1 binding were sheared for 20 mins using a rheometer at a high rotary stress (6 Pa) (n=4-7 independent samples per group). Low shear indicates a rotary stress the carrier erythrocyte experienced during rotation using a revolver at 12 rpm/min. Data in are presented as mean ± s.e.m.. n.s.: not significantly different (two-way ANOVA followed by Tukey's HSD test).

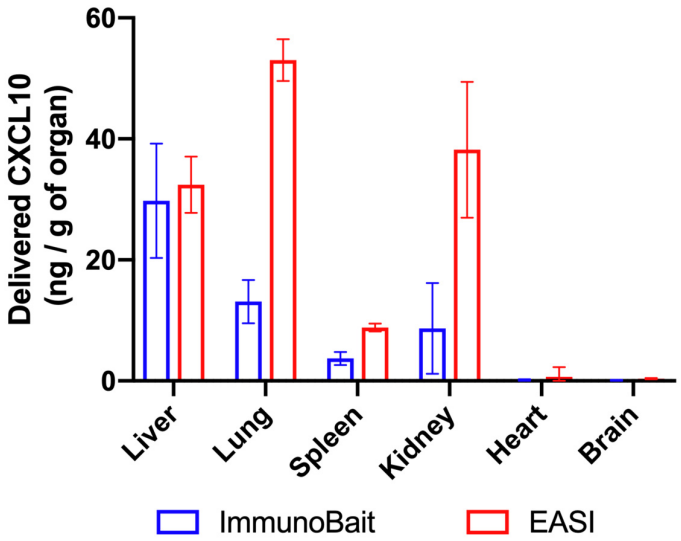

Fig. S9. Organ distribution of delivered CXCL10 chemokine quantified by ELISA
Healthy Balb/c Mice (n=5 biologically independent animals per group) were administered with ImmunoBait (coated with anti-ICAM-1 antibody) or EASI formulation intravenously. 20 mins after injection, mice were euthanized and major organs were collected. Organs were homogenized and processed. CXCL10 concentration was detected by ELISA and basal level of CXCL10 in blank mice (n=5 biologically independent animals per group) was used as a control. Data are presented as mean ± s.e.m.

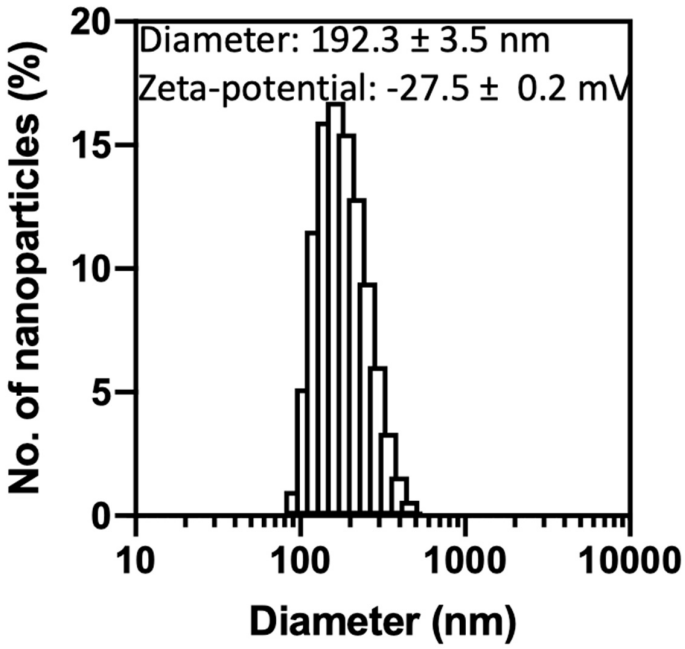

Fig. S10. Physicochemical properties of ImmunoBait coated with anti-ICAM-1 antibody

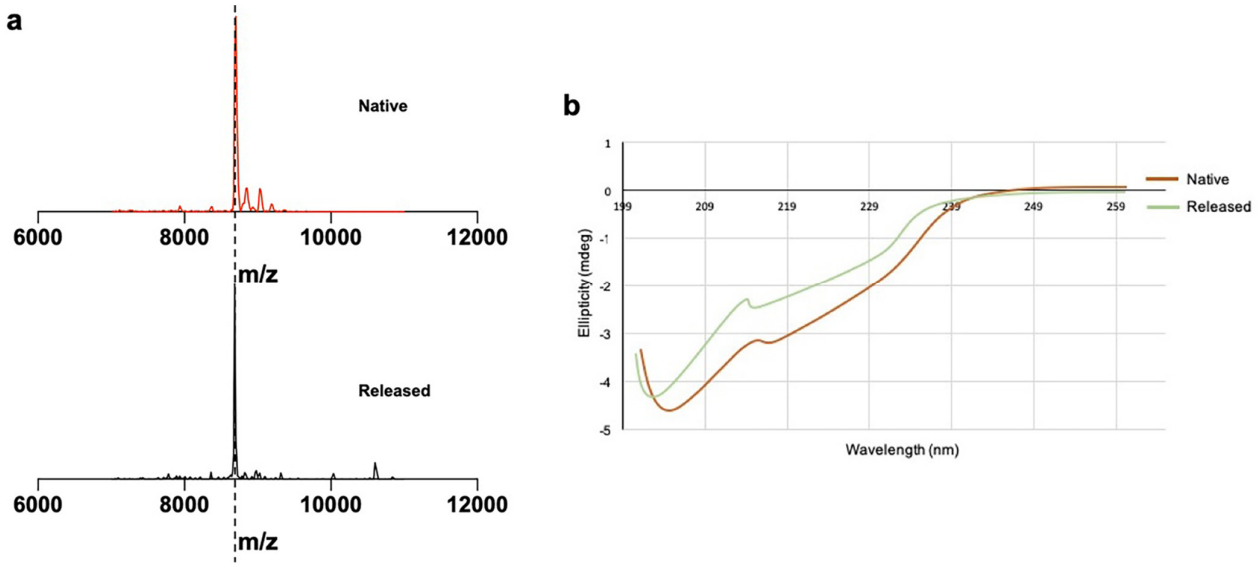

Fig. S11. Stability of CXCL10 following encapsulation into ImmunoBait

(**a**) MALDI-TOF spectrum of native CXCL10 and CXCL10 released from ImmunoBait. (**b**) Circular Dichroism Spectrum of native CXCL10 and CXCL10 released from ImmunoBait.

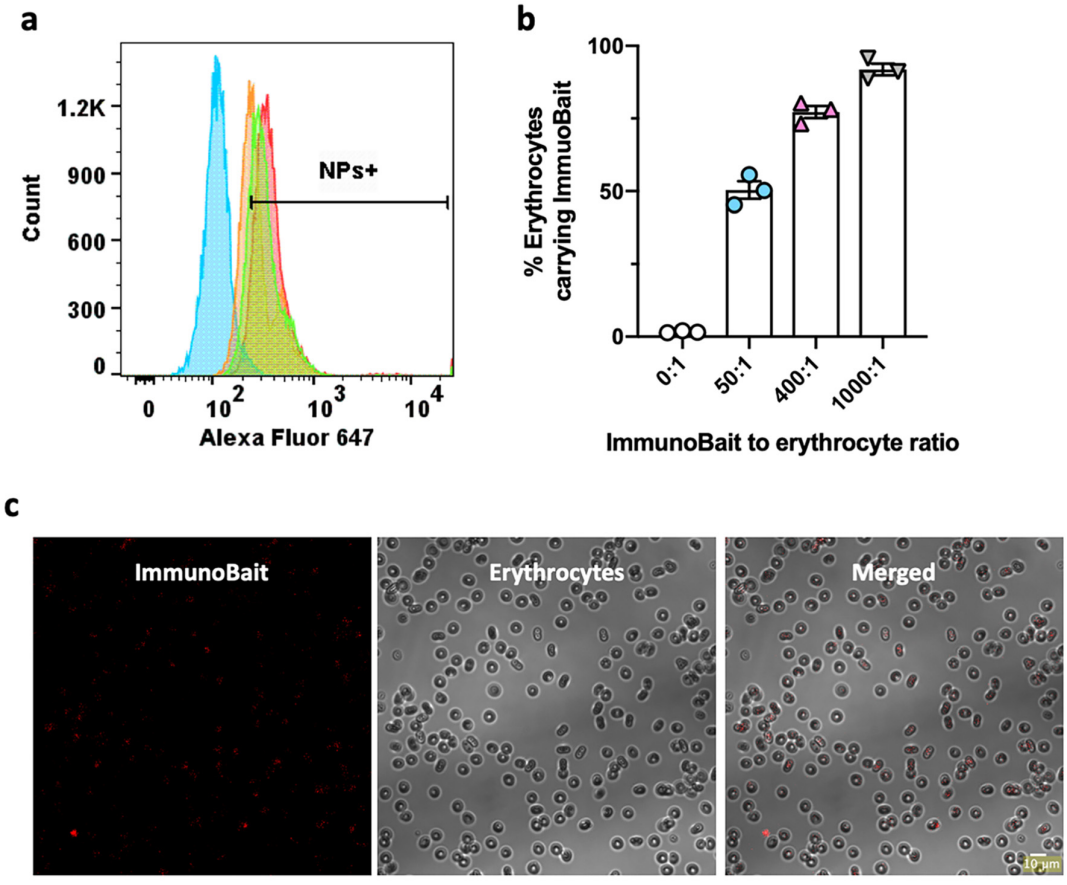

Fig. S12. Assembly of ImmunoBait onto the surface of mouse erythrocytes

(**a**) Flow cytometry histogram plots of erythrocytes after being incubated with different amount of ImmunoBait nanoparticles. ImmunoBait to erythrocyte ratios used in histograms from left to right are 0:1, 50:1, 400:1, and 1000:1, respectively. (**b**) Percentage of erythrocytes carrying ImmunoBait nanoparticles after being incubated at different ImmunoBait to erythrocyte ratios (n=3 independent samples per group). Data

are presented as mean ± s.e.m. (**c**) CLSM images of erythrocytes carrying ImmunoBait nanoparticles when being incubated at a ImmunoBait to erythrocyte ratio of 400:1. In (**a**-**c**), ImmunoBait was labeled by Alexa Fluor 647 which was conjugated to the encapsulated chemokine.

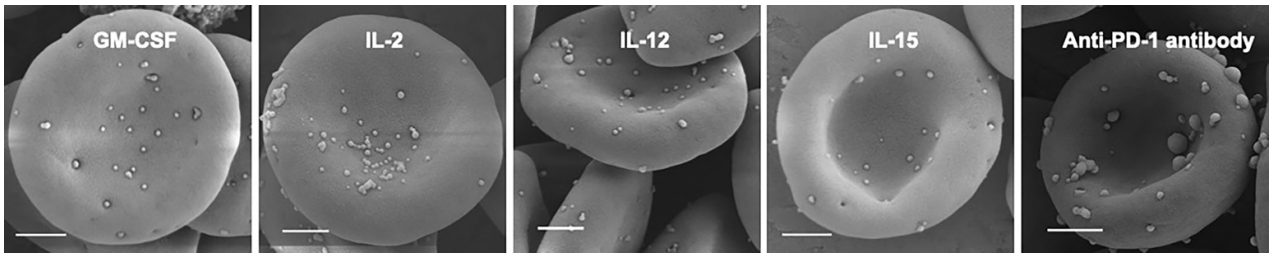

Fig. S13. Assembly of ImmunoBait carrying other immunomodulatory agents onto erythrocytes
GM-CSF, IL-2, IL-12, and IL-15 were encapsulated in ImmunoBait. Anti-PD-1 antibody was conjugated to the surface of ImmunoBait. Scale bar: 1 μm.

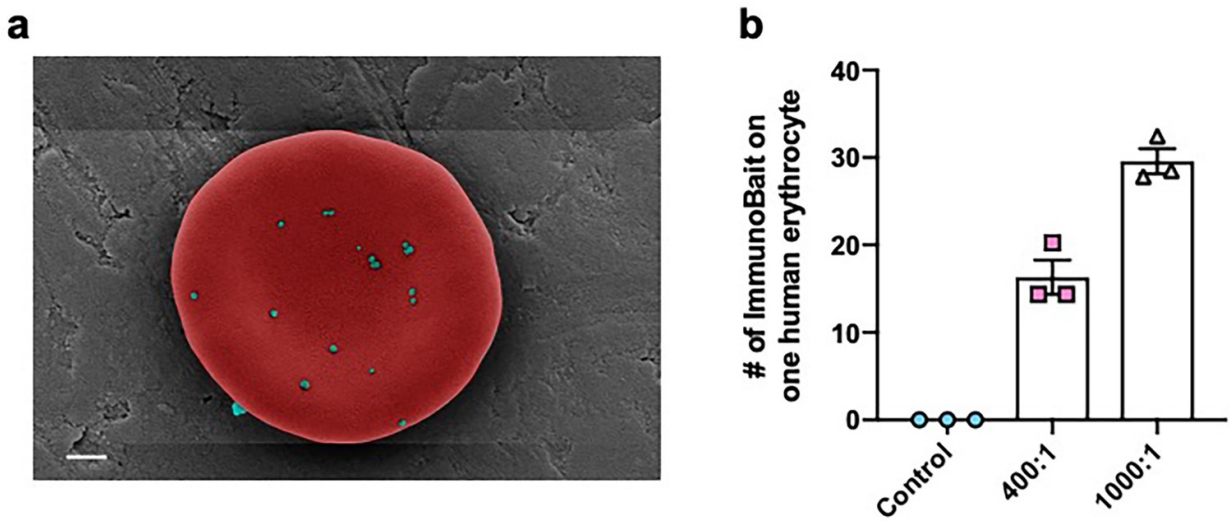

Fig. S14. Assembly of ImmunoBait to human erythrocytes
(**a**) SEM images of human erythrocytes with ImmunoBait nanoparticles assembled on them. Scale bar: 1 µm. (**b**) Number of ImmunoBait nanoparticles assembled onto the surface of human erythrocytes at different ImmunoBait to human erythrocyte incubation ratios (n=3 independent samples per group). Data are presented as mean ± s.e.m.

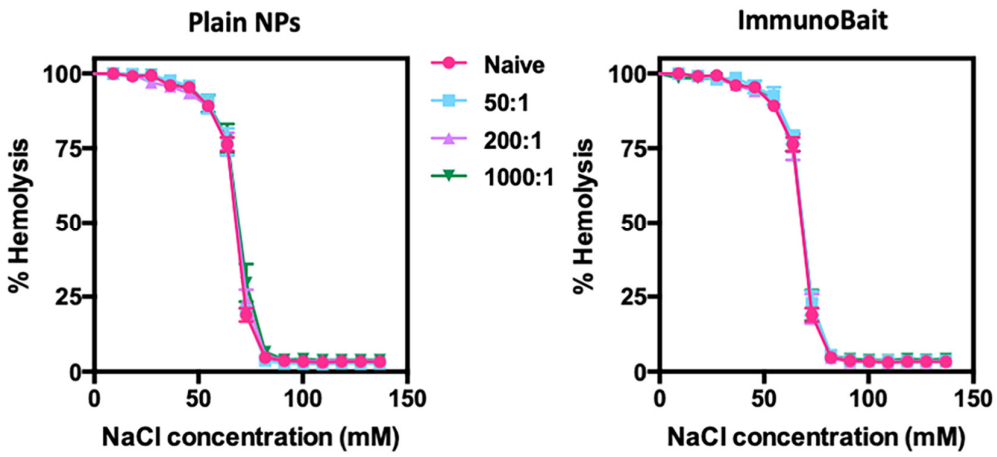

Fig. S15. Impact of ImmunoBait hitchhiking on the sensitivity of the carrier erythrocytes to osmotic stress Representative osmotic fragility curves of carrier erythrocytes were shown (n=3 independent samples per group). The carrier erythrocytes at all the tested nanoparticle concentrations exhibited similar fragility curves compared to Naive erythrocytes. Data are presented as mean ± s.e.m.

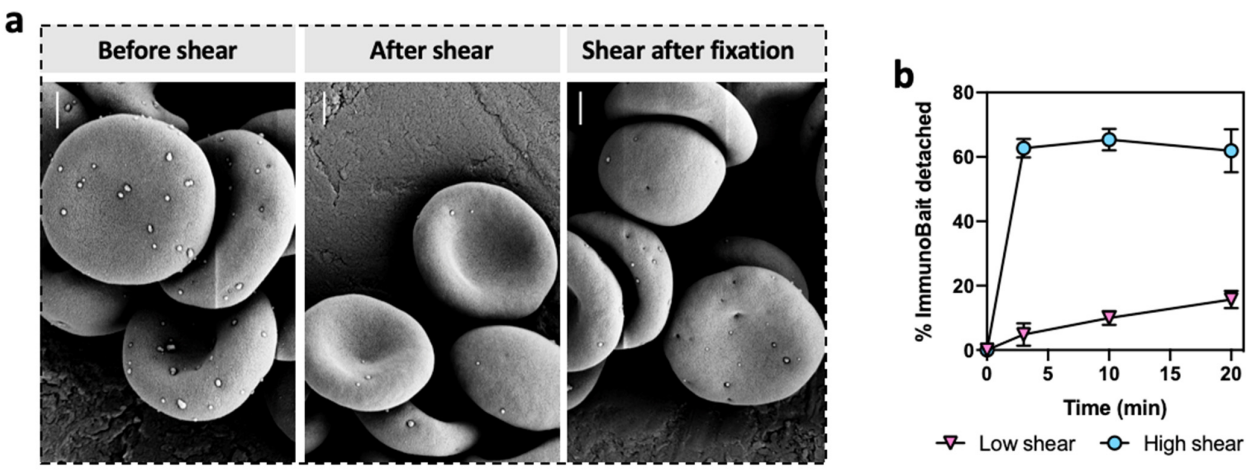

Fig. S16. ImmunoBait was released from carrier erythrocytes under shear

(**a**) SEM images of ImmunoBait hitchhiked erythrocytes before shear, after shear, or shear after fixation. Samples were sheared at a rotary shear stress of 6 Pa for 20 mins. (**b**) Percent ImmunoBait nanoparticles detached from the carrier erythrocytes when being sheared at low shear stress (rotary shear at 12 rpm) or high shear stress (6 Pa) for 3, 10, or 20 mins (n=3 independent samples per group). Data in (**b**) are presented as mean ± s.e.m.

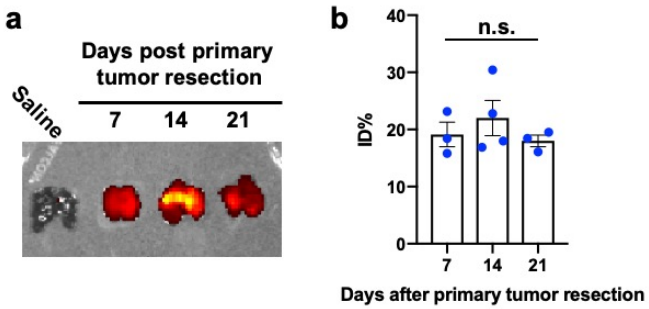

Fig. S17. Lung accumulation of ImmunoBait delivered by EH with the progression of lung metastasis
On days 7, 14, and 21 after primary tumour resection, different sets of mice were IV administered with EASI with aICAM-1 (n=3-4 biologically independent animals per group). 20 mins after injections, mice were euthanized and organs were collected for fluorescence measurement using IVIS. ImmunoBait NPs were labeled by encapsulating Alexa Fluor 647-Ovalbumin. (**a**) Representative IVIS images of lungs. (**b**) ID% of ImmunoBait NPs accumulated in the lungs. Data indicated that with the progression of lung metastasis, the amount of NPs delivered to lungs by erythrocyte hitchhiking remained similar. Not significantly different among all groups (One-way ANOVA followed by Tukey's HSD test): n.s. Data are presented as mean ± s.e.m.

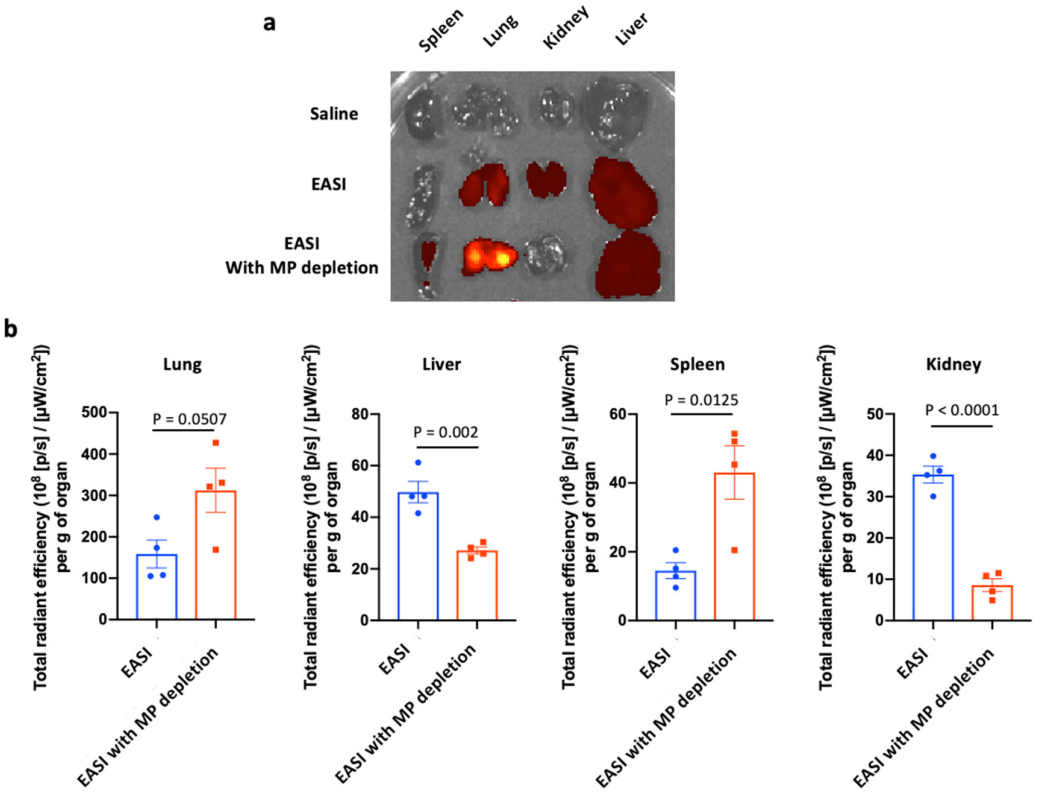

Fig. S18. ImmunoBait Nanoparticles delivered to metastatic lungs by erythrocyte hitchhiking were not entrapped in phagocytes

Phagocytes (mainly tissue macrophages) were depleted by IV administration of 200 µL of Clodrosome® containing 5 mg/mL Clodronate 48 h before IV injection of EASI. ImmunoBait NPs were labeled by encapsulating Alexa Fluor 647-Ovabumin. 20 min after EASI administration, mice (n=4 biologically independent animals per group) were euthanized and major organs including lung, liver, spleen, and kidney were collected and imaged using IVIS. Fluorescence intensity (radiant efficiency) of ROI was quantified and analyzed. (**a**) Representative IVIS images of organs of mice injected with saline, EASI, or EASI after phagocyte depletion. (**b**) Total radiant efficiency per gram of organ in major organs of mice with or without phagocyte depletion. The depletion of phagocytes resulted in reduced NP accumulation in the liver and kidney, indicating NPs accumulated in these two organs were majorly entrapped in phagocytes. In contrast, the accumulation of NPs in the lung was not decreased when phagocytes were depleted, suggesting the detached ImmunoBait NPs in the lung were not majorly entrapped in phagocytes. Data are presented as mean ± s.e.m. Statistical analysis in (**b**): two-tailed student's t test.

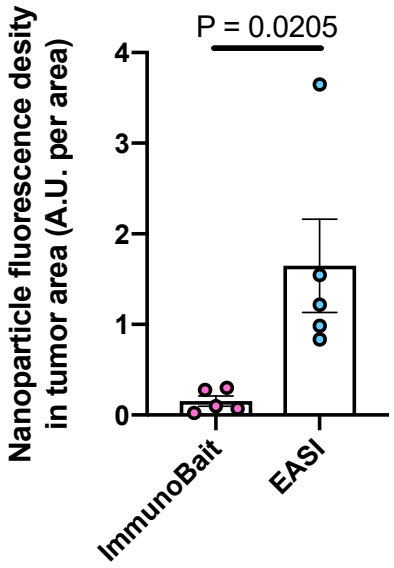

Fig. S19. Semi-quantitative comparison of the accumulation of nanoparticles in the tumor
Nanoparticle fluorescence density (A.U. per area) in the tumor area was calculated from confocal images as represented in Fig. 3e.

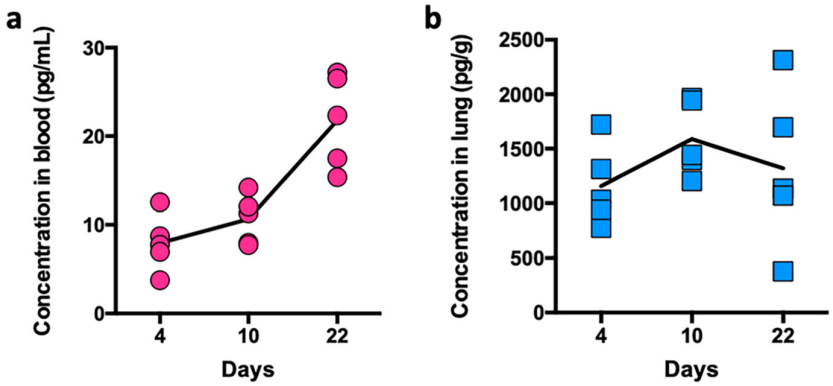

Fig. S20. Concentrations of the CXCL10 chemokine in the blood and lung of mice bearing breast cancer lung metastasis at different time after primary tumour resection

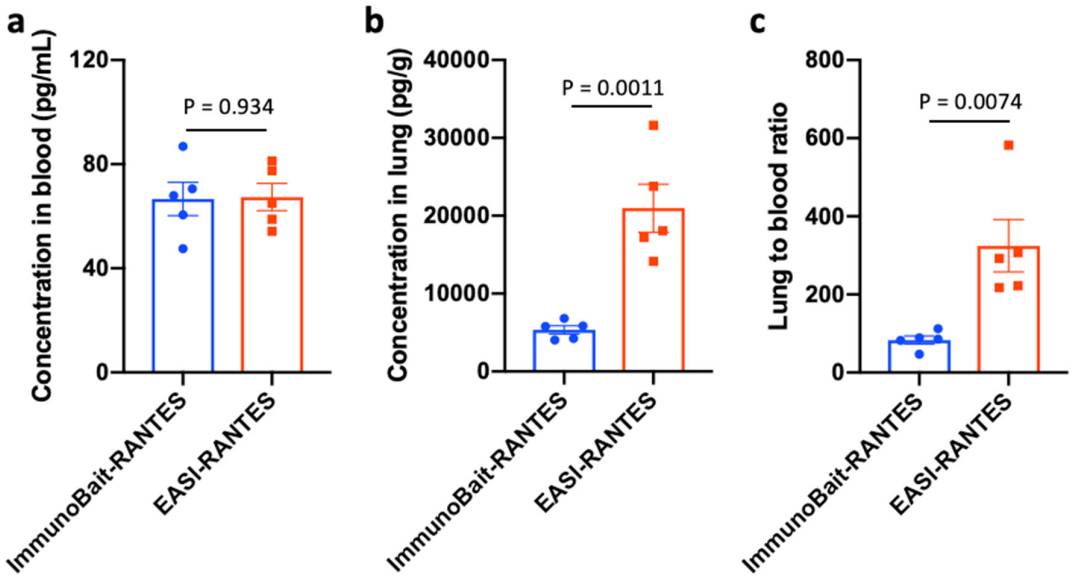

Fig. S21. Delivery of RANTES (a chemokine) by erythrocyte hitchhiking

ImmunoBait-RANTES was prepared by encapsulating RANTES in PLGA nanoparticles. Anti-ICAM-1 antibody was coated to ImmunoBait-RANTES. 6 h after IV administration of formulations, RANTES concentrations in the serum and lung homogenates were quantified by ELISA. (**a**) Concentration of RANTES chemokine in the blood (n=5). (**b**) Concentration of RANTES chemokine in the lung (n=5). (**c**) Lung to blood ratio of RANTES chemokine concentration after administration (n=5). Data are presented as mean ± s.e.m. Each dot in each graph represents data from biologically independent animals. Statistical analysis: two-tailed student's t test.

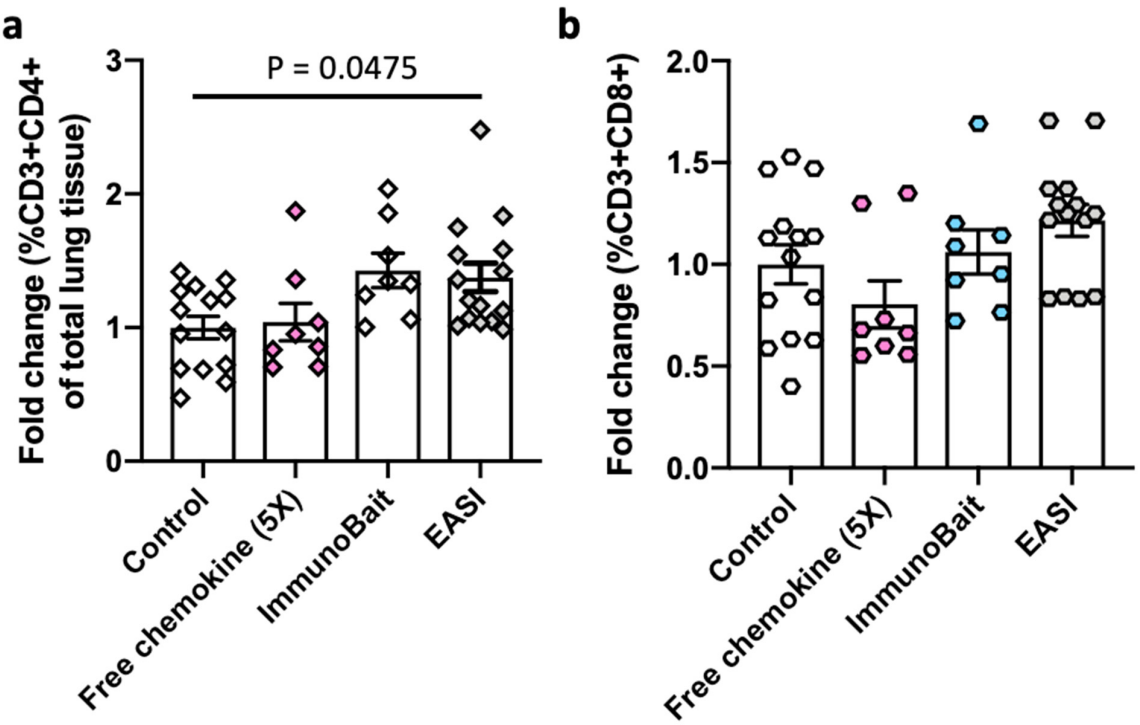

Fig. S22. Immune cells in the metastatic lungs of mice under different treatments
The absolute percentage of (**a**) CD4 (CD3+CD4+) and (**b**) CD8 (CD3+CD8+) cells in the lungs were shown. Data are presented as mean ± s.e.m. Each dot in each graph represents data from biologically independent animals. Statistical analysis: One-way ANOVA followed by Tukey's HSD test.

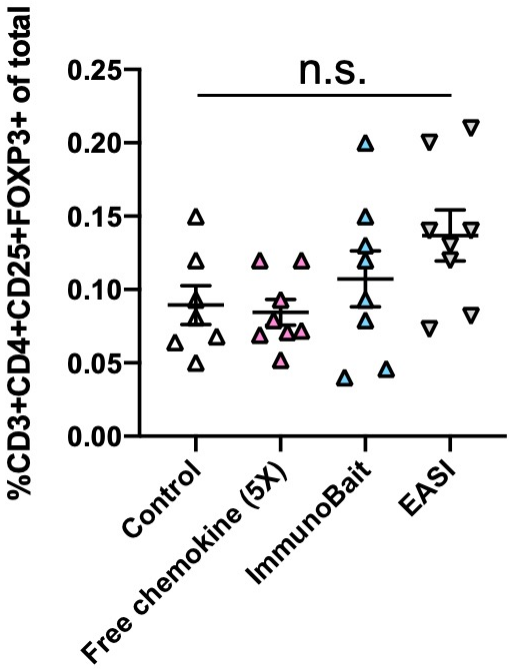

Fig. S23. Absolute percentage of regulatory T cells (CD3+CD4+CD25+FOXP3+ cells) in the metastatic lungs following therapy by different treatments

Data are presented as mean ± s.e.m. Each dot represents data from biologically independent animals. Not significantly different among all groups (One-way ANOVA followed by Tukey's HSD test): n.s.

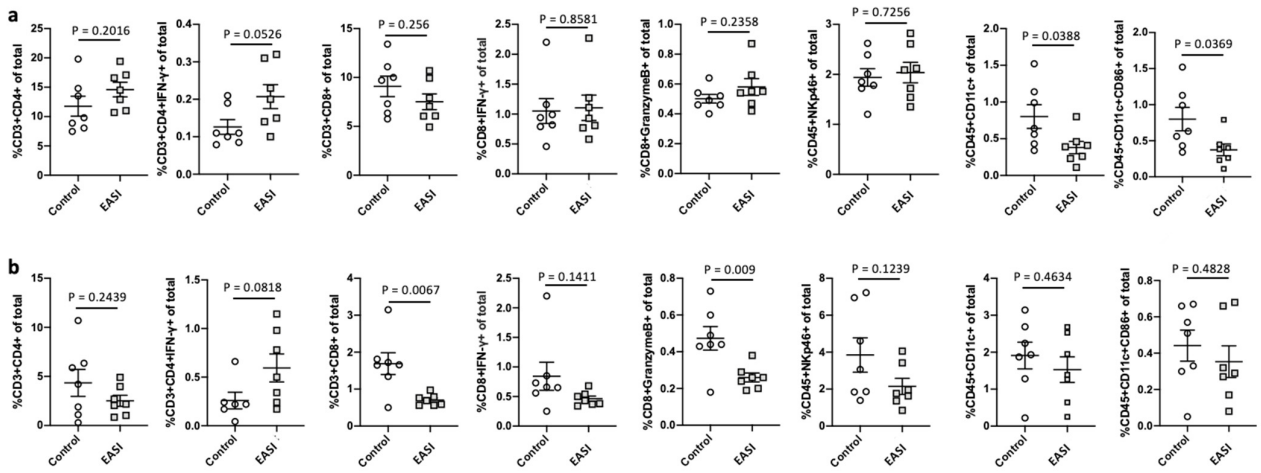

Fig. S24. Immune cells in different organs of mice under different treatments

The absolute percentage of CD4 cells (CD3+CD4+), Th1 CD4 cells (CD3+CD4+IFN-γ+), CD8 cells (CD3+CD8+), effector CD8 cells (CD8+IFN-γ+ and CD8+GranzymeB+), NK cells (CD45+NKp46+), dendritic cells (CD45+CD11c+), and activated dendritic cells (CD45+CD11c+CD86+) in the (**a**) spleen and (**b**) liver were shown. Data are presented as mean ± s.e.m. Each dot in each graphrepresents data from biologically independent animals. Statistical analysis: two-tailed student's t test.

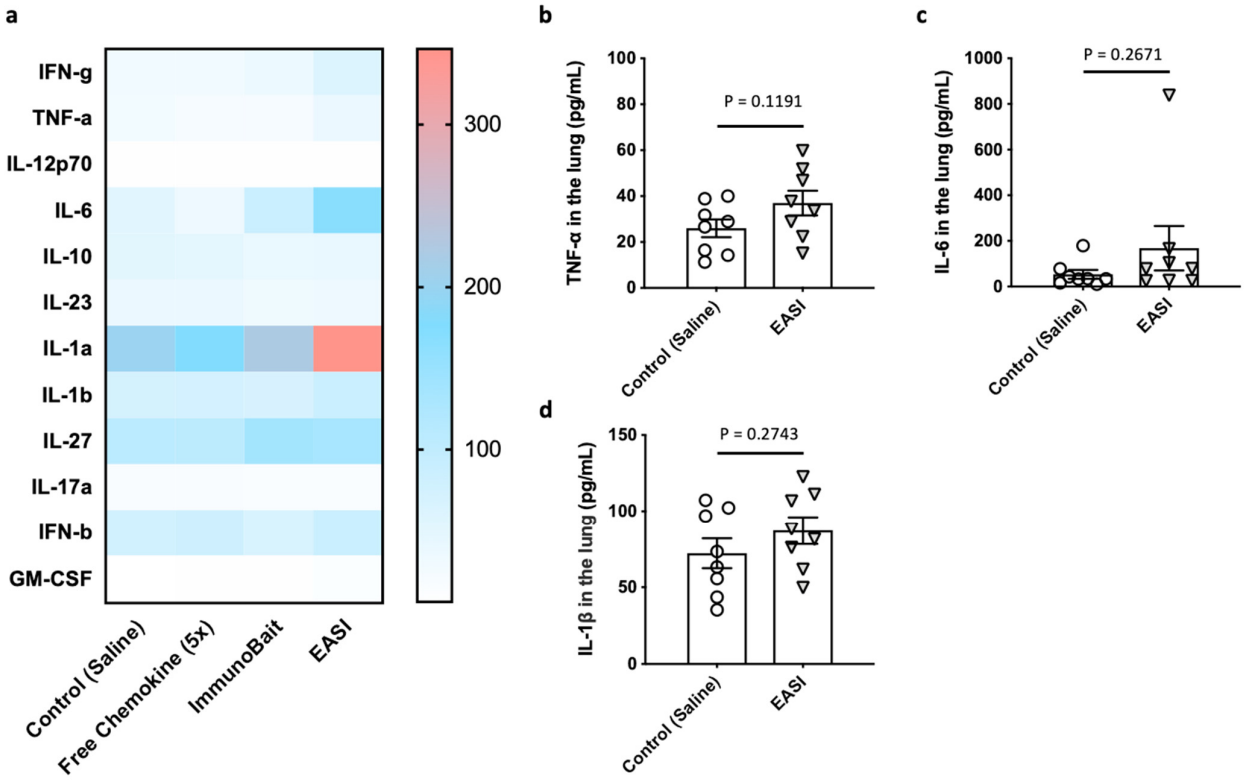

Fig. S25. Cytokine profiles of lungs having 4T1-Luc metastasis following different treatments

(**a**) Heat-map showing the concentrations of cytokines in the metastatic lungs of mice being treated by different treatments. Unit: pg/mL. Comparisons between saline and EASI treated groups in terms of acute inflammatory cytokine levels of (**b**) TNF-α, (**c**) IL-6, and (**d**) IL-1β were performed. Data in (**b**) are part of these in Fig. 5k. Data in (**b**-**d**) are presented as mean ± s.e.m. Each dot represents data from biologically independent animals. Statistical analysis: two-tailed student's t test.

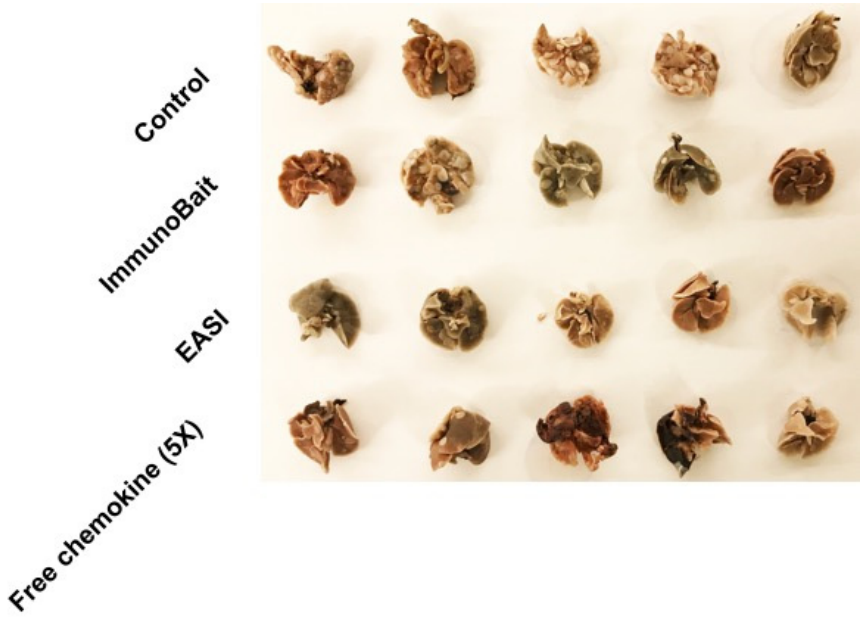

Fig. S26. Representative images of the back side of lungs of mice on day 37 under different treatments in the early-stage 4T1-Luc lung metastasis model

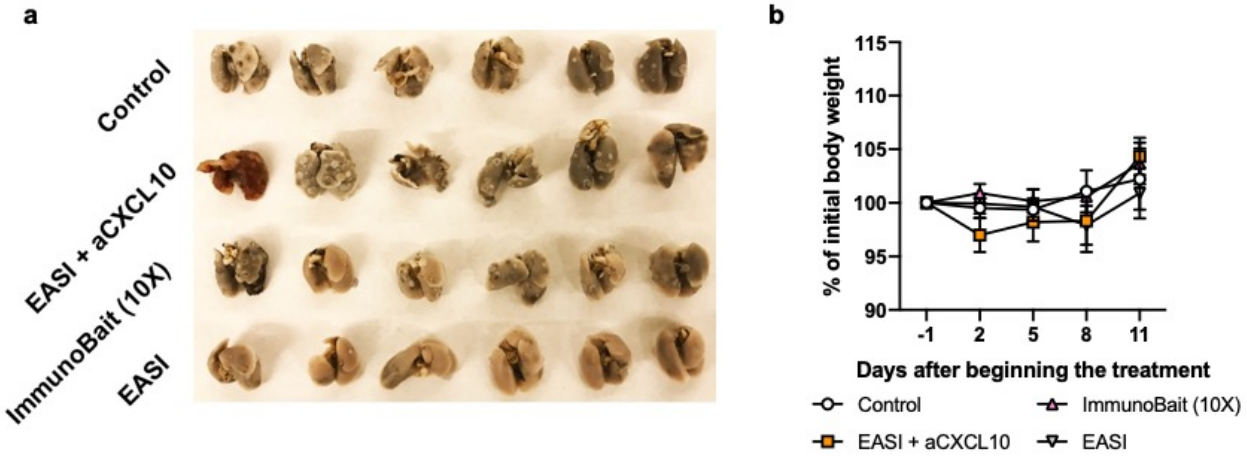

Fig. S27. Efficacy and safety evaluation of different formulations in inhibiting 4T1-Luc lung metastasis progression

(**a**) Representative images of lungs of mice on day 37 under different treatments in the early-stage 4T1-Luc lung metastasis model. (**b**) Body weight change of mice during the treatment. Data in (**b**) are presented as mean ± s.e.m.

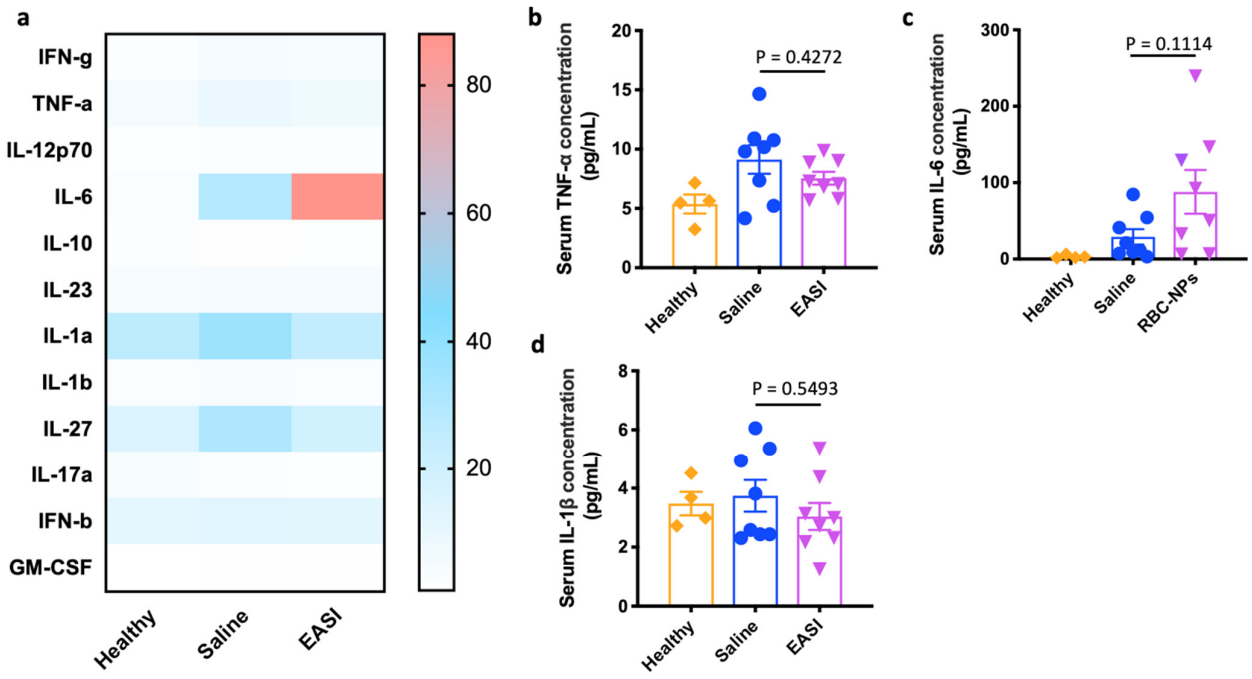

Fig. S28. Serum cytokine profiles of mice having 4T1-Luc metastasis following different treatments
(**a**) Heat-map showing the concentrations of cytokines in the serum of mice being treated by different treatments. Unit: pg/mL. Comparisons between saline and EASI treated groups in terms of acute inflammatory cytokine levels of (**b**) TNF-α, (**c**) IL-6, and (**d**) IL-1β were performed. Data in (**b**-**d**) are presented as mean ± s.e.m. Each dot represents data from biologically independent animals. Statistical analysis: two-tailed student's t test.

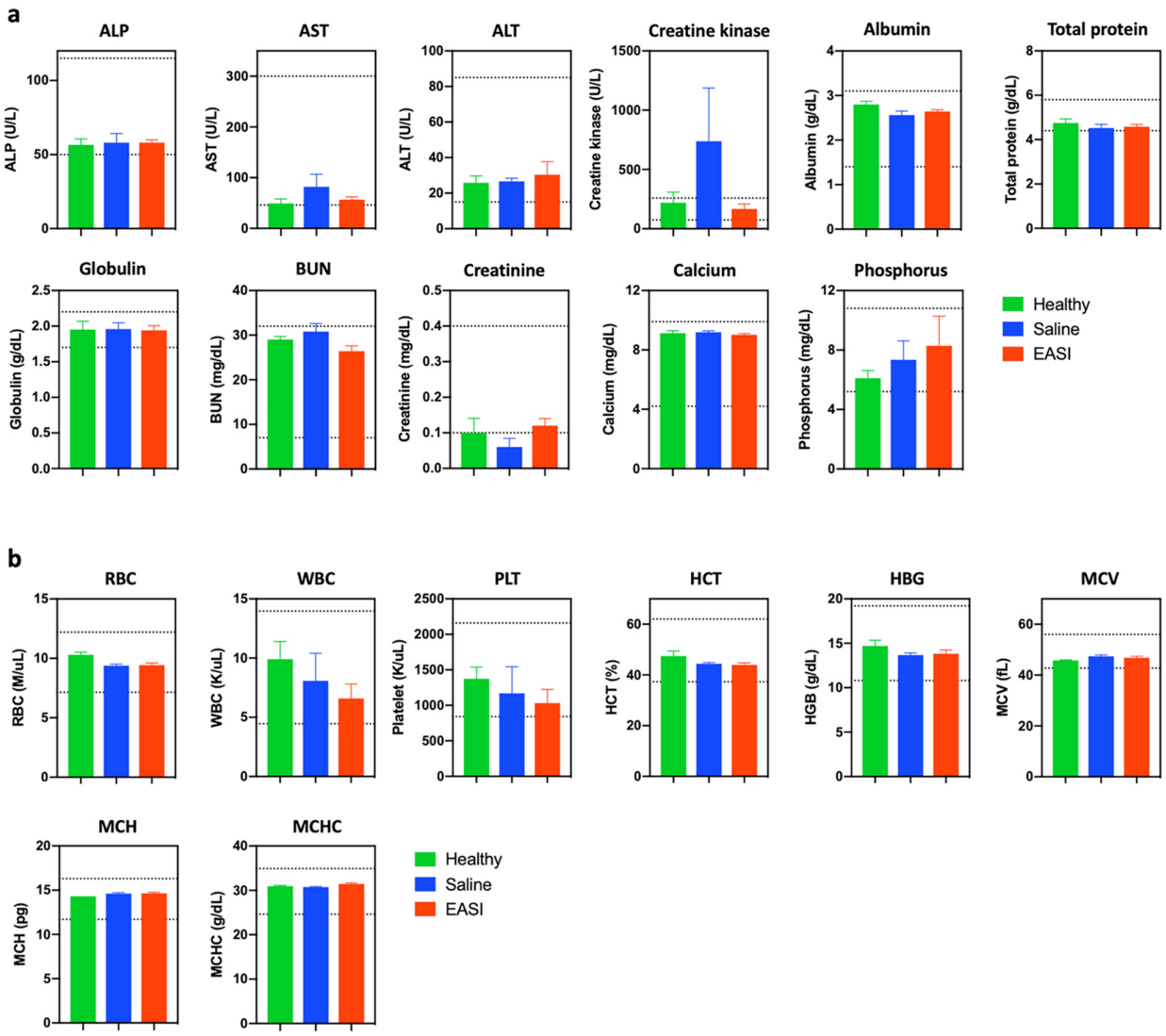

Fig. S29. Serum chemistry and hematology analysis of mice bearing B16F10-Luc lung metastasis following 4 doses of EASI treatments

(**a**) Serum chemistry data. No significantly differences between the Saline group and EASI group were detected for any of the serum chemistry parameters (One-way ANOVA followed by Tukey's HSD test). ALP: alkaline phosphatase, AST: aspartate aminotransferase, ALT: alanine aminotransferase, BUN: blood urine nitrogen. (**b**) Hematology data. No significantly differences between the Saline group and EASI group were detected for any of the hematological parameters (One-way ANOVA followed by Tukey's HSD test). RBC: red blood cell, WBC: white blood cell, PLT: platelet, HCT: hematocrit and RET, HBG: hemoglobin, MCV: mean corpuscular volume, MCH: mean corpuscular hemoglobin, MCHC: mean corpuscular hemoglobin concentration. In (**a**-**b**), n=5 biologically independent animals per group for Saline and EASI while n=4 biologically independent animals for Healthy. Data are presented as mean ± s.e.m. Dashed Lines indicate established normal range.

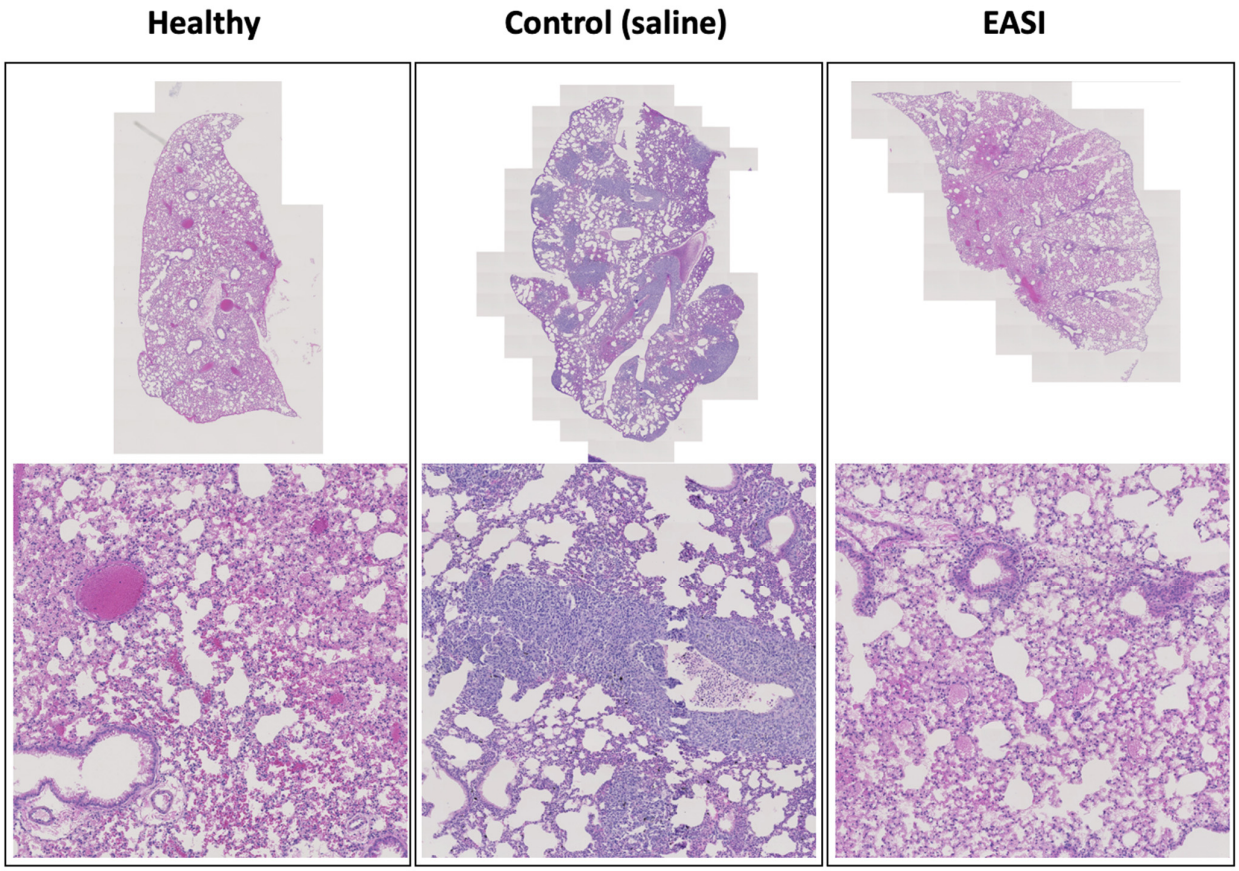

Fig. S30. H&E of lungs of mice bearing 4T1-Luc lung metastasis following different treatments in the early-stage lung metastasis model

For the Control (saline) and EASI group, mice received same doses (4 doses) of formulations as in the efficacy study (Fig. 6). Lungs of mice were analyzed by H&E staining. Age-matched healthy mice without any formulation administration were used as control. No obvious damage to healthy lung tissue in the EASI group was observed. Representative of n=8 biologically independent animals per group.

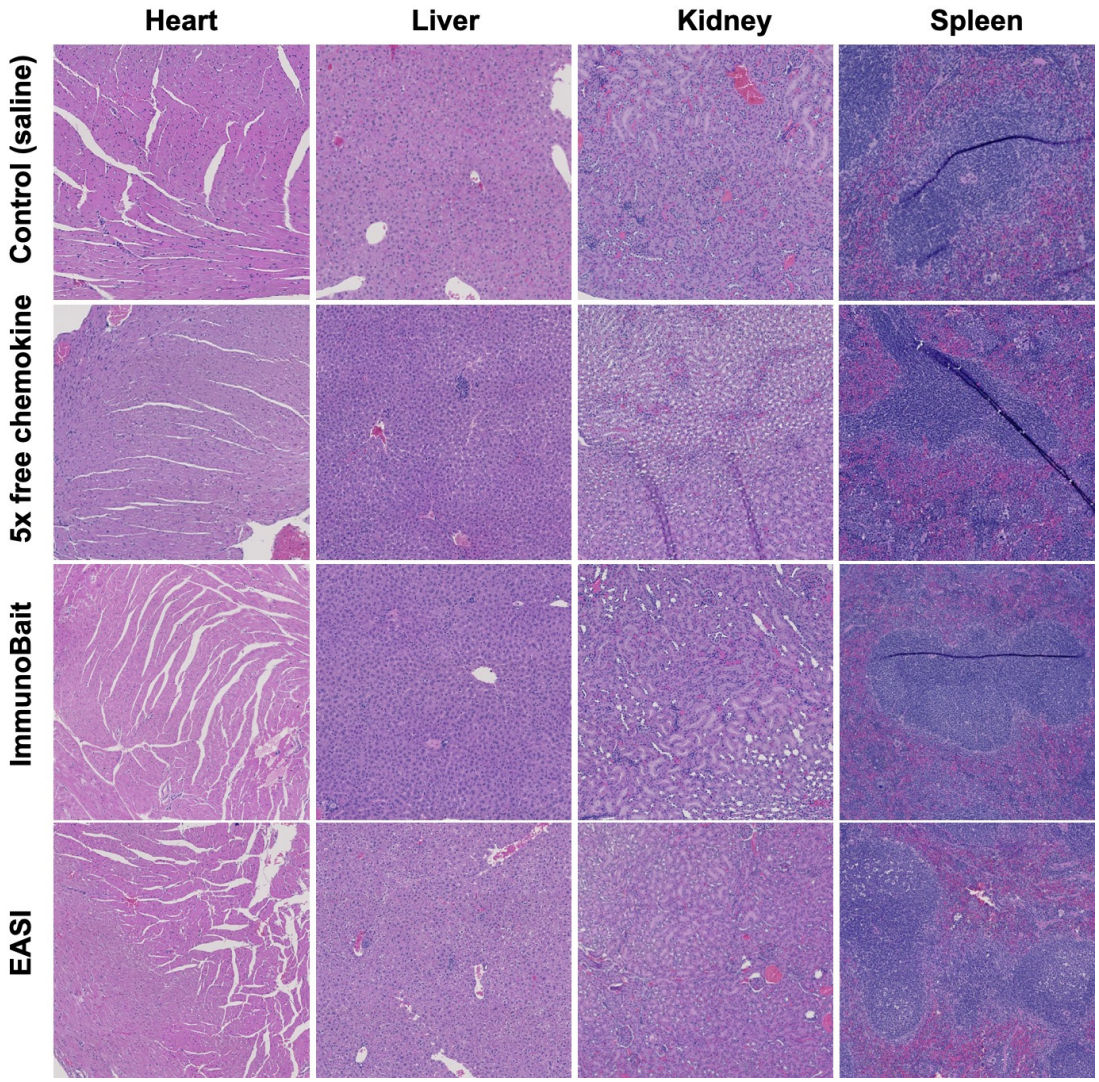

Fig. S31. H&E of mouse organs following different treatments in the 4T1-Luc early-stage lung metastasis model

Mice received same doses (4 doses) of formulations as in the efficacy study (Fig. 6). Organs of mice were analyzed by H&E staining. Representative of n=8 biologically independent animals per group.

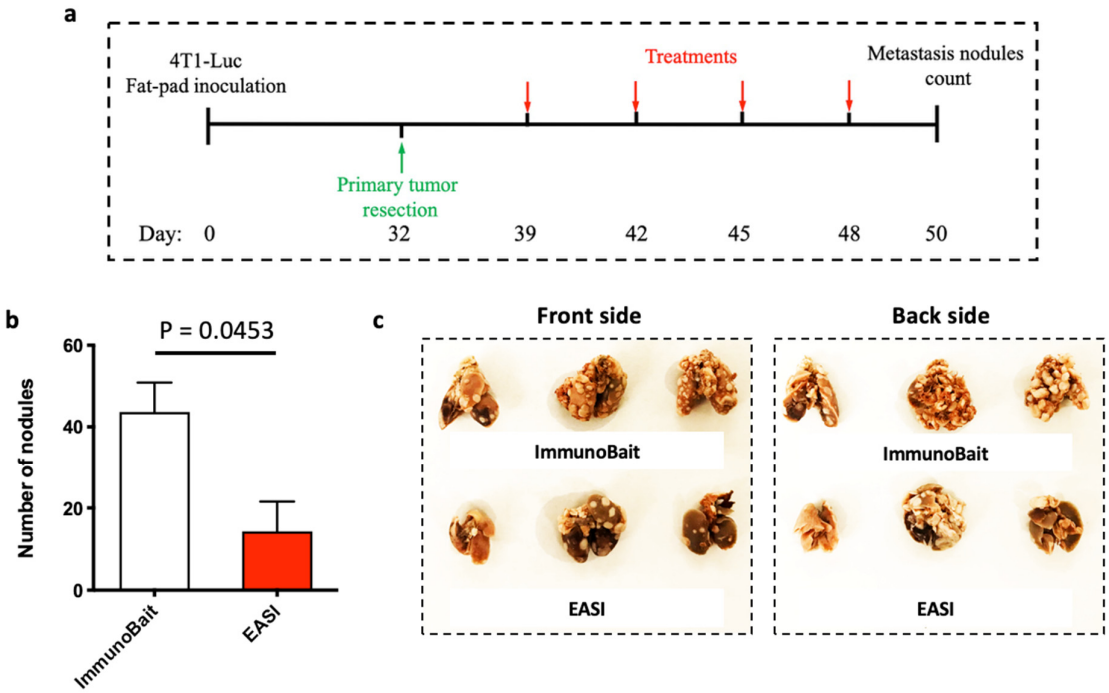

Fig. S32. Efficacy of EASI in inhibition of 4T1-Luc lung metastasis in a late-stage breast cancer lung metastasis model

(**a**) Schedule for the efficacy study in the late-stage lung metastasis model. (**b**) Nodule number on excised lungs of mice on day 50 following different treatments (n=3 biologically independent animals per group). Statistical analysis: two-tailed student's t test. Data are presented as mean ± s.e.m. (**c**) Images of excised lungs on day 50.

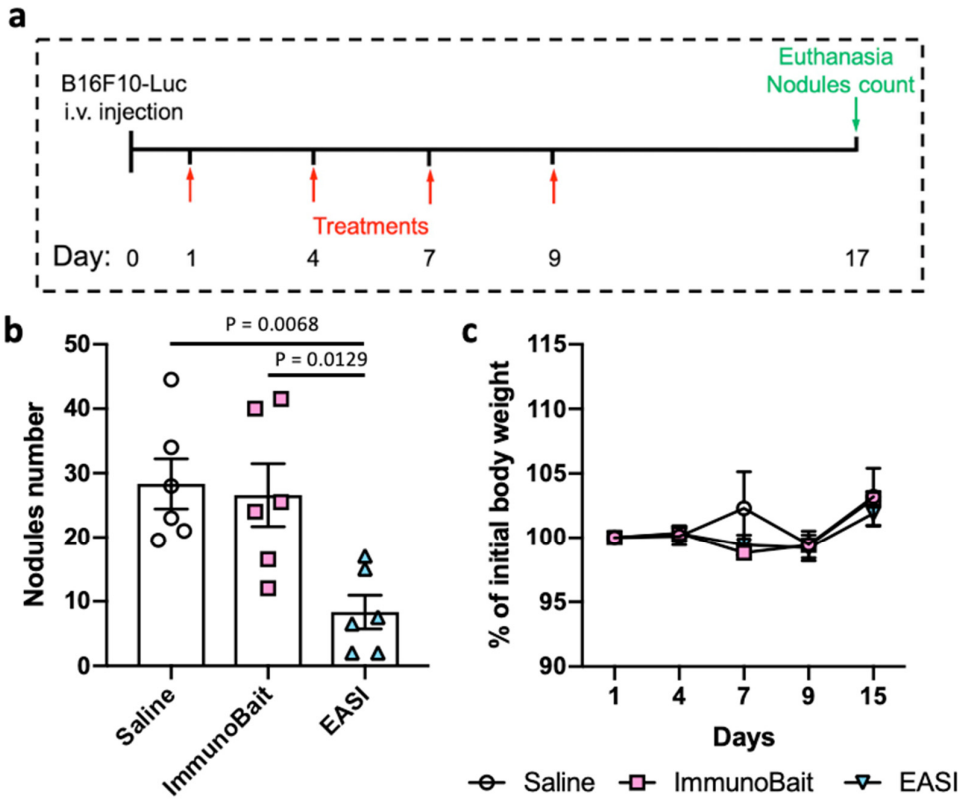

Fig. S33. Efficacy of EASI in inhibition of lung metastasis in a B16F10-Luc melanoma lung metastasis model (**a**) Schedule for the efficacy study in the B16F10-Luc melanoma lung metastasis model. (**b**) Nodule number on excised lungs of mice on day 17 following different treatments (n=6 biologically independent animals per group). Statistical analysis: One-way ANOVA followed by Tukey's HSD test. (**c**) Body weight of mice during the study. Data in (**b-c**) are presented as mean ± s.e.m.

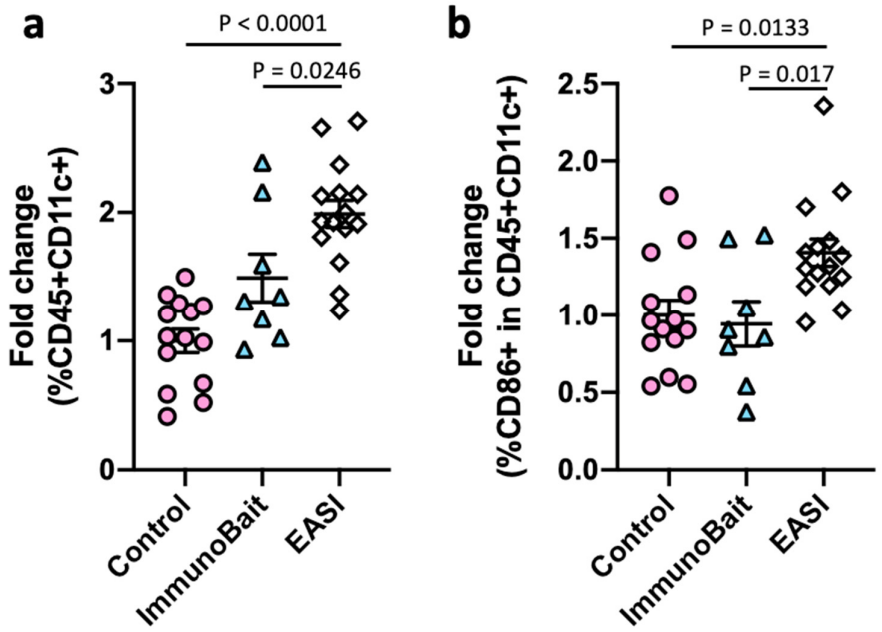

Fig. S34. Dendritic cells in the lungs of mice bearing 4T1 lung metastasis under different treatments
(**a**) The fold-change of the absolute percentage of dendritic cells (CD45+CD11c+) in the lungs. (**b**) The fold-change of the percentage of CD86+ cell in CD45+CD11c+ dendritic cells. Each dot represents data from biologically independent animals. Data are presented as mean ± s.e.m. Statistical analysis in (**a, b**): One-way ANOVA followed by Tukey's HSD test. n=8-15 biologically independent animals per group.

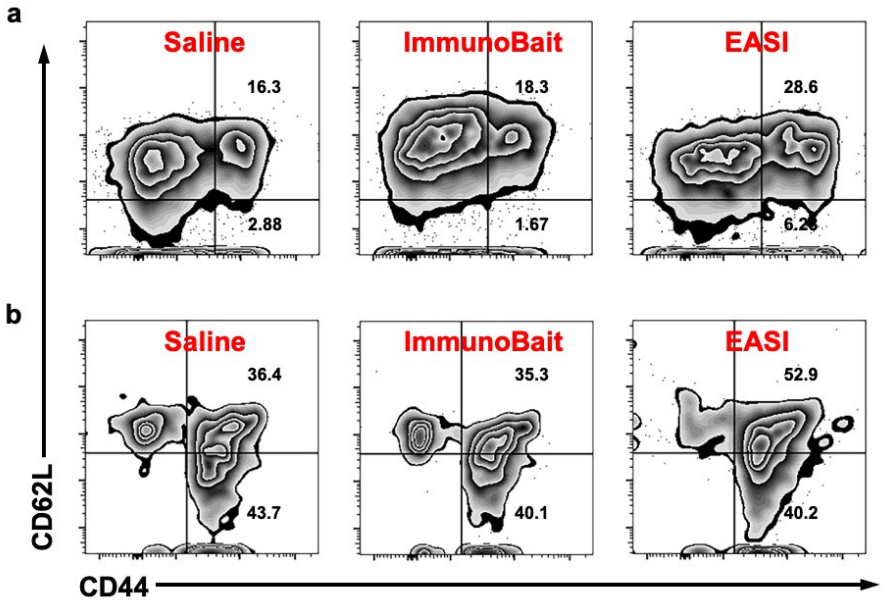

Fig. S35. Memory CD8 cells in the blood and spleen after the treatment by EASI
(**a**) Representative flow cytometry analysis images of CD8+CD62L+CD44+ cells and CD8+CD62-CD44+ cells in the blood (gated on CD8+ cells). (**b**) Representative flow cytometry analysis images of CD8+CD62L+CD44+ cells and CD8+CD62L-CD44+ cells in the spleen (gated on CD8+ cells). Representative of n=7 biologically independent animals per group.

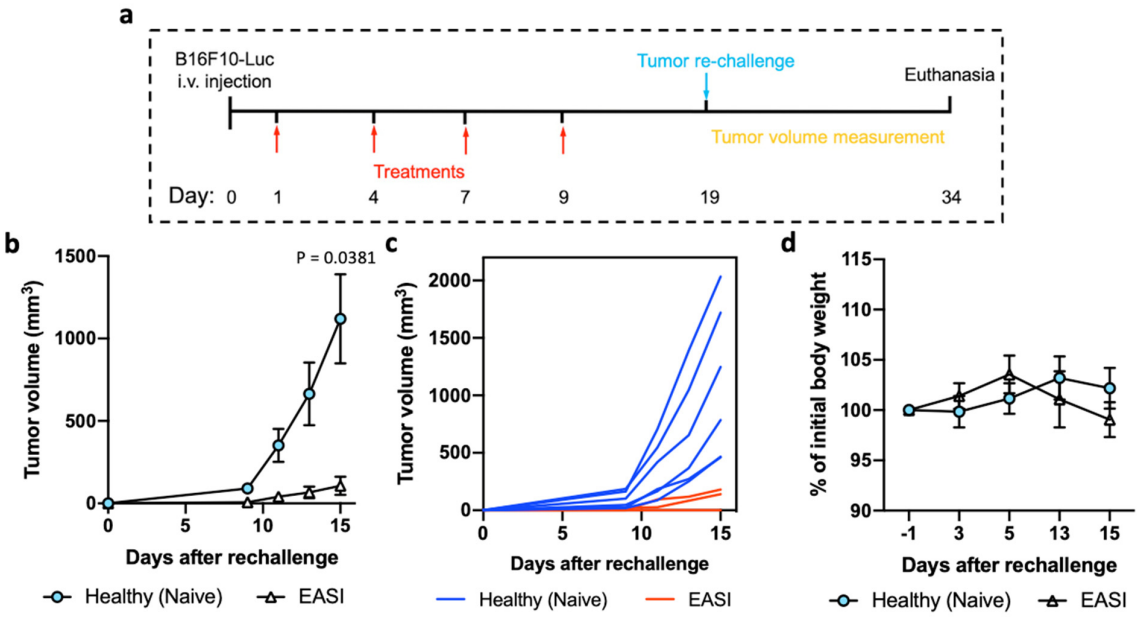

Fig. S36. Efficacy of EASI in inhibition of re-challenged tumours in a B16F10-Luc melanoma lung metastasis model

(**a**) Schedule for the re-challenge study in the B16F10-Luc melanoma lung metastasis model. (**b**) Overall growth curve of re-inoculated tumours (n=6 biologically independent animals for the Healthy (Naïve) group and n=3 biologically independent animals for the EASI group). Mice bearing lung metastasis that were treated by saline or ImmunoBait died before a palpable tumour could be seen. 3 out of 6 mice in the EASI group died or were euthanized because of euthanasia endpoint requirements before palpable tumours were seen. Statistical analysis: two-tailed student's t test. (**c**) Tumour growth curve of individual mice. Each line represents the tumour growth curve of one individual mice. (**d**) Body weight of mice during the study. Data in (**b-d**) are presented as mean ± s.e.m.

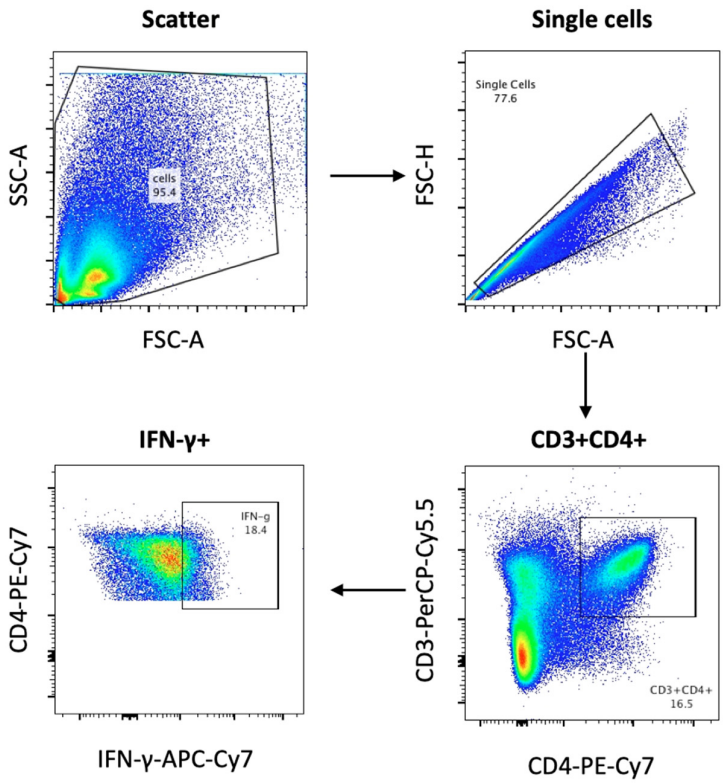

Fig. S37. Representative flow cytometry gating strategies for IFN-γ+ CD4 cells

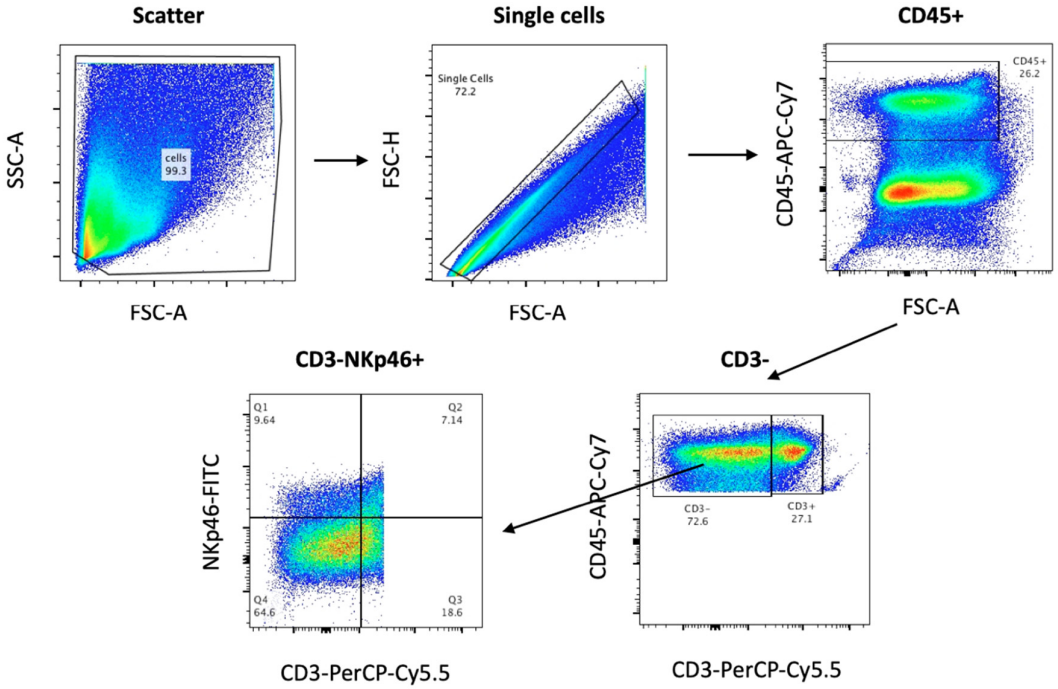

Fig. S38. Representative flow cytometry gating strategies for NKp46+ NK cells

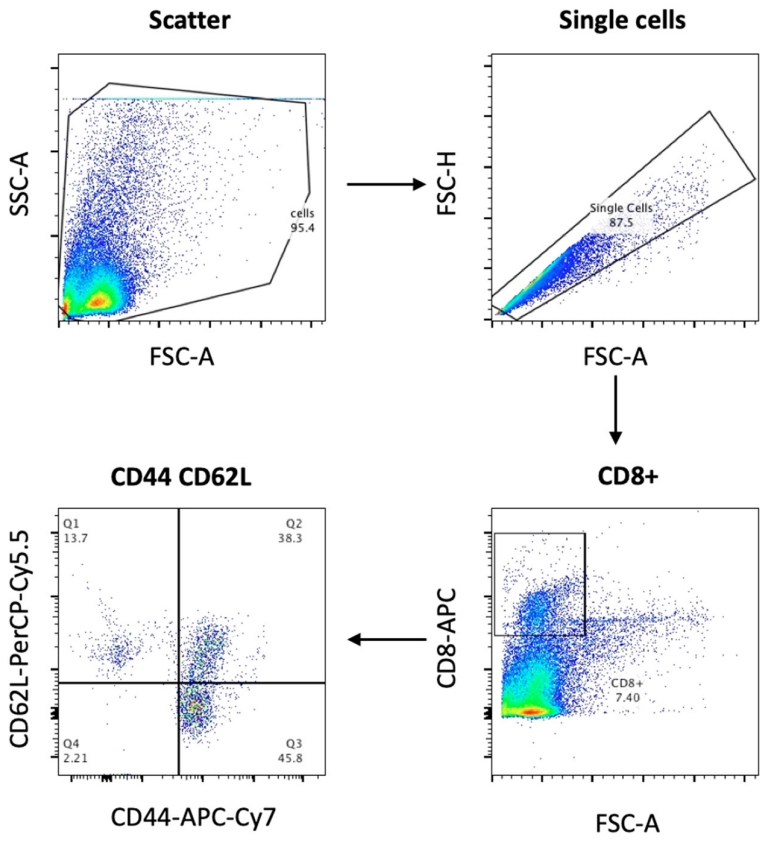

Fig. S39. Representative flow cytometry gating strategies for memory CD8 cells

References for Supplementary Information

1. Chambers, E. & Mitragotri, S. Long circulating nanoparticles via adhesion on red blood cells: mechanism and extended circulation. *Exp Biol Med (Maywood)* **232**, 958-966 (2007).
2. Pan, D. et al. The Effect of Polymeric Nanoparticles on Biocompatibility of Carrier Red Blood Cells. *PLoS One* **11**, e0152074 (2016).
3. Miretti, S. et al. A Mouse Model of Pulmonary Metastasis from Spontaneous Osteosarcoma Monitored In Vivo by Luciferase Imaging. *Plos One* **3** (2008).
4. Zhao, Z., Ukidve, A., Gao, Y., Kim, J. & Mitragotri, S. Erythrocyte leveraged chemotherapy (ELeCt): Nanoparticle assembly on erythrocyte surface to combat lung metastasis. *Sci Adv* **5**, eaax9250 (2019).
5. Brenner, J.S. et al. Red blood cell-hitchhiking boosts delivery of nanocarriers to chosen organs by orders of magnitude. *Nat Commun* **9** (2018).